American Mineralogist, Volume 85, pages 633–648, 2000

Th-Pb ion-microprobe dating of allanite

E.J. Catlos,[1,*] Sorena S. Sorensen,[2] and T. Mark Harrison[1]

[1]Department of Earth and Space Sciences and Institute of Geophysics and Planetary Physics, University of California, Los Angeles, California 90095-1567, U.S.A.
[2]Department of Mineral Sciences, NHB-119, National Museum of Natural History, Smithsonian Institution, Washington, D.C. 20560, U.S.A.

Abstract

Allanite, which is a common accessory mineral in a wide variety of rock types, typically contains high concentrations of Th and U; thus, an in-situ method of U-Th-Pb dating of this phase would have broad application. We describe a method to permit Th-Pb ages of allanite to be determined with approximately ±10% accuracy using a high-resolution ion microprobe. Knowledge of the composition and substitution mechanisms of this complex mineral is key to understanding the relative ionization efficiencies of Th^+ and Pb^+. The chemical compositions of three allanite samples used as age standards (Cima d'Asta Pluton, 275.5 ± 1.5 Ma; Atesina Volcanic Complex, 276.3 ± 2.2 Ma; La Posta Pluton, 94 ± 2 Ma) were determined using an electron microprobe, permitting an assessment of matrix effects on ionization. An ion-microprobe calibration curve involving elemental and oxide species of Th and Pb (i.e., $^{208}Pb^*/Th^+$ vs. ThO_2^+/Th^+) yields highly scattered apparent ages when allanite age standards with different Fe contents are used. However, a three-dimensional plot of $^{208}Pb^*/Th^+$ vs. ThO_2^+/Th^+ vs. FeO^+/SiO^+ improves the accuracy of the calibration to about ±10%. Even though this level of uncertainty is substantially greater than that expected for U-Th-Pb ion-microprobe analyses of zircon or monazite, Th-Pb ages of allanite can still be used to address important geologic questions.

We used this method to date two metamorphic allanite grains from the footwall of the Main Central Thrust, Nepal Himalaya, and an allanite grain from the Pacoima Canyon pegmatite, California. Allanite inclusions in garnet from Nepal yield significantly older ages than the coexisting monazite, indicating that allanite formation in these rocks records a previous metamorphic cycle that predates slip along the fault. The Pacoima Canyon allanite grain yields a younger age than that reported for zircon, implying Pb loss during cooling of the pegmatite.

Introduction

Allanite occurs primarily in regionally metamorphosed pelites and felsic igneous rocks. An epidote group mineral [$A_2M_3Si_3O_{12}(OH)$], allanite preferentially incorporates Th and U into its structure and has been used for U-Th-Pb dating studies using isotope dilution methods (Mezger et al. 1989; von Blackenburg 1992; Davis et al. 1994; Barth et al. 1994a; Oberli et al. 1999). Using an ion microprobe to determine allanite U-Th-Pb ages would have several advantages over conventional methods: mineral separation is not needed, dating of small grains (~15 μm) is feasible, and textural relationships are preserved permitting inclusion/host relationships to be assessed. The ion microprobe is especially useful because it has the spatial resolution to analyze small areas of allanite that are least affected by damage resulting from α-decay events (metamictization) and subsequent alteration

In the allanite structure (see above generalized formula), the A sites (A1 and A2) contain large, highly coordinated cations, such as Ca^{2+}, Sr^{2+}, or REE^{3+}, whereas the M sites (M1, M2, and M3) contain octahedrally coordinated cations, such as Al^{3+}, Fe^{3+}, Mn^{3+}, Fe^{2+}, or Mg^{2+} (Dollase 1971). However, allanite may also contain relatively large amounts of other elements, including Th^{4+}, U^{4+}, Zr^{4+}, P^{5+}, Ba^{2+}, and Cr^{3+} (see Deer et al. 1993). The potentially high degree of compositional variability makes allanite a challenging phase for ion-microprobe dating because significant matrix effects on the ionization efficiency of U, Th, and Pb could restrict the use of even well-characterized standards to a narrow compositional range. For example, U-Pb ages can routinely be determined for zircon [$Zr(SiO_4)$] with a precision of ±1% (Compston 1999), whereas precision of Th-Pb ages of monazite [$(LREE,Th)PO_4$] appears to be restricted to ±2% (Harrison et al. 1995). This higher level of uncertainty may reflect the greater potential for compositional substitution in monazite (e.g., 0–15 wt% ThO_2; Deer et al. 1993).

In this paper, we document the limitations imposed by matrix effects on the relative ionization of Th^+ and Pb^+ in dating allanite using a conventional ion-microprobe calibration plot. We then develop a method involving FeO^+/SiO^+ as a proxy control on the matrix effects, which permit us to determine the Th-Pb ages of compositionally characterized allanite to an accuracy of approximately ±10%. The application of this method is illustrated by dating metamorphic allanite from the Nepal Himalaya and igneous allanite from a Californian pegmatite.

Allanite petrogenesis

The chemistry of epidote-group minerals varies mainly in the A2 and M3 sites. Allanite and epidote are related by the coupled substitution $REE^{3+} + Fe^{2+} = Ca^{2+} + Fe^{3+}$. A major dif-

*E-mail: catlos@argon.ess.ucla.edu

ference between the two minerals is that ideal allanite contains only Fe^{2+} in the M sites, whereas end-member epidote contains Fe^{3+} (Burt 1989). The coupled substitution can be inferred from electron-microprobe analyses of allanite from a variety of rocks including garnet amphibolite from the Catalina Schist, southern California (Sorensen 1991), granitoid rocks from the Western Carpathians, Slovakia (Petrík et al. 1995), and igneous, metamorphic, and hydrothermally altered rocks from the Isle of Skye, Scotland (Exley 1980).

Backscattered electron (BSE) images of allanite grains typically show internal zoning controlled by the abundance of light rare-earth elements (LREE), Fe, Th, and U (for examples see Sorensen 1991; Buda and Nagy 1995; Petrík et al. 1995; and this paper). Zoning of the LREE in allanite has been attributed to a complex interplay between geochemical environment, coupled substitutions, and mineral-structure constraints. For example, Affholter (1987) synthesized allanite grains under controlled P, T, and f_{O_2}, and found that Fe^{2+} in the M3 site expands the allanite structure to accommodate LREE in the A2 site. Affholter (1987) concluded that natural allanite grains with epidote rims reflect REE control indirectly related to f_{O_2} and suggested that if the environment were to become more oxidizing at a fixed P and T, epidote could form rather than allanite. In some hydrothermal allanite grains, Fe^{2+}/Fe^{3+} decreases from LREE-rich cores to LREE-depleted, heavy REE-enriched rims (see Exley 1980). Sawka et al. (1984) interpreted similar LREE zoning of allanite grains in granitoid rocks to result from changes in the melt composition during differentiation and solidification. Sorensen (1991) interpreted changes of LREE fractionation and abundance in hydrothermal LREE-enriched epidote grains to reflect changes in fluid composition.

Several investigators have explored the significance of epidote as an indicator of the minimum intrusion pressure of granodioritic and tonalitic magmas (Zen and Hammarstrom 1984; Dawes and Evans 1991; Schmidt and Thompson 1996). Magmatic allanite is commonly found in cores of epidote crystals and may be stable to higher temperatures than is common for epidote (Schmidt and Thompson 1996). Gieré et al. (1999) speculated that the stability of allanite in magmatic environments may be closely related to temperature and f_{H_2} rather than to the REE content of the melt or a threshold pressure. Franz et al. (1986) showed that allanite is stable under conditions of eclogite formation. Experiments using basaltic-andesite, andesite, and rhyodacite glasses doped with REE contained stable allanite at 1050 °C and 30 kbar (Green and Pearson 1983). Crystalline allanite also formed in experiments run with trondhjemite glass + 50% H_2O at 900 °C and 20 kbar (Adams et al. 1996). Hydrothermally synthesized, end-member Ce-allanite breaks down to britholite, anorthite, magnetite, quartz, and a Ce-silicate at 800 °C, 1 kbar, and 0.25 X_{H_2O} (Affholter 1987). Although allanite appears to be more common in rocks of the greenschist facies than of higher grades (Overstreet 1967), the P-T stability of allanite in metamorphic rocks is estimated from its textural relationship with monazite breakdown (Smith and Barriero 1990; Finger et al. 1998).

From petrologic observations, monazite appears to form at the staurolite isograd (~500 °C) in pelitic rocks from allanite breakdown reactions (Smith and Barreiro 1990; Kingsbury et al. 1993; Wing et al. 1999). In metaluminous orthogneisses, magmatic allanite destabilizes to monazite and thorite at higher temperatures (700–760 °C; Bingen et al. 1996). Monazite is typical of peraluminous granitoid rocks, whereas allanite is reported mainly from more CaO-rich metaluminous granitoid rocks (Broska and Siman 1998). Lee and Bastron (1967) reported that granites with <0.7 wt% CaO contain monazite but not allanite, whereas granites with >1.8 wt% CaO contain only allanite. In pelitic schists, allanite and monazite coexist in rocks with CaO concentrations of <0.5 wt% (Smith and Barreiro 1990).

METHODS

Ion-microprobe dating of allanite

The CAMECA ims 1270 ion microprobe can be used to determine U-Pb ages of zircon and Th-Pb ages of monazite with precisions of 1–2% at a spatial resolution of ~15 µm (see Harrison et al. 1995; Quidelleur et al. 1997; Harrison et al. 1999). Like monazite, allanite preferentially incorporates Th during growth, which results in relatively high contents of radiogenic ^{208}Pb. The allanite grains in this study contain ThO_2 concentrations up to 1.8 wt% and low common Pb concentrations suggesting that the mineral potentially can be dated using the ion microprobe. However, allanite poses a challenge for ion-microprobe analysis because ionization efficiencies of Th^+ and Pb^+ appear to be highly sensitive to compositional variations (see Reed 1985, 1986). In addition, matrix effects associated with Fe-bearing minerals have been reported (Havette 1985). For example, sputtering yields of Mg^+ in both olivine and Ca-poor pyroxene (Shimizu et al. 1978) and the Ca^+/Si^+ ratio of pyroxene appear to increase as a function of Fe^+ intensity (Shimizu and LeRoex 1986).

Individual grains of allanite were mounted in epoxy, polished using 0.3 mm alumina, and coated with carbon. A 2–4 nA primary O^- beam focused to a 15 × 20 mm spot produced a high ionization efficiency of Pb from allanite. The analyses were done using a 50 eV energy window, a ~10eV offset for Th^+, and a mass resolving power of ~6000. At this mass resolution, all Pb and Th isotopes were resolved from any significant molecular interferences (Fig. 1). The energy distributions for $^{232}Th^+$, $^{248}ThO^+$, $^{264}ThO_2^+$, and $^{208}Pb^+$ ions sputtered from the allanite are similar to those of monazite (Fig. 2; see Harrison et al. 1995).

Age dating using the ion microprobe takes advantage of the kinetic energy distribution of sputtered ions of Th and Pb (Harrison et al. 1995). Three isotope ratios are measured: $^{264}ThO_2^+/^{232}Th^+$, $^{208}Pb^+/^{232}Th^+$, and $^{204}Pb^+/^{208}Pb^+$. The $^{208}Pb^+/^{232}Th^+$ is corrected for common Pb using the relationship $^{208}Pb^*/^{232}Th^+ = (^{208}Pb^+/^{232}Th^+)\{1-[(^{208}Pb/^{204}Pb)_S(^{204}Pb^+/^{208}Pb^+)]\}$, where $(^{208}Pb/^{204}Pb)_S$ is the known ratio of the standard. (The asterisk indicates the species is corrected for common Pb.) As described by Harrison et al. (1995), a linear relationship exists between $^{208}Pb^*/^{232}Th^+$ and $^{264}ThO_2^+/^{232}Th^+$ for monazite grains with known uniform Pb/Th ratio. Isotopic data collected from several ion-microprobe spots on the monazite age standard define this linear relationship, and allow derivation of a correction factor determined by dividing the measured $^{208}Pb^+/^{232}Th^+$ of a stan-

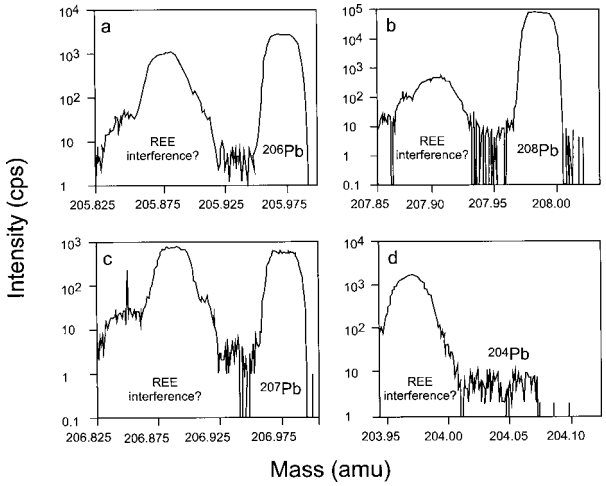

FIGURE 1. Plots of ion intensity [in counts per second (cps)] for allanite as measured with the ion microprobe. At a mass resolving power of ~6000, the (**a**) ^{206}Pb, (**b**) ^{208}Pb, and (**c**) ^{207}Pb peaks are distinctly separated from probable rare-earth silicate interferences. This allanite had very little common lead (**d**).

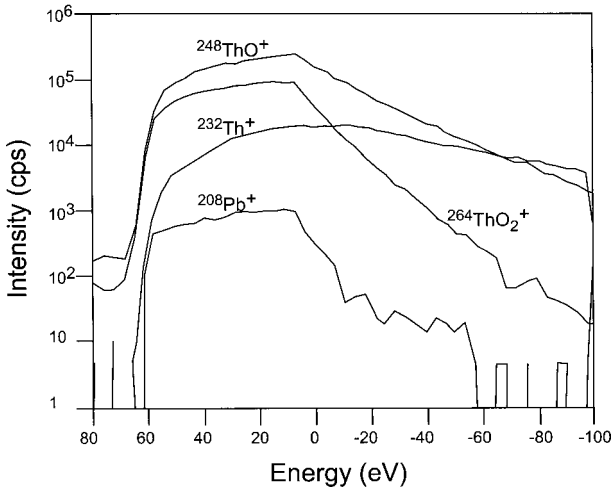

FIGURE 2. Kinetic energy distribution of $^{264}ThO_2^+$, $^{248}ThO^+$, $^{208}Pb^+$, and $^{232}Th^+$ sputtered from allanite using the ion microprobe with a primary oxygen ion beam.

dard grain at a reference $^{264}ThO_2^+/^{232}Th^+$ value by its known daughter-to-parent ratio. This correction factor, permits the determination of Pb/Th ratios of unknown grains measured under the same instrumental conditions. For ion-microprobe analyses of 20 Ma monazite grains, the precision of the 2-D calibration method is limited not by counting statistics, but by the reproducibility of the calibration curve (typically ±2%; Harrison et al. 1995).

In this study, we used three materials as allanite Th-Pb dating standards. Two of the three are from a calc-alkaline, volcanoplutonic association in the Southern Alpine domain, Northern Italy. Using U-Th-Pb isotope-dilution methods, Barth et al. (1994a) dated single grains of these samples. Studies by Barth et al. (1994b) indicate that Pb was not lost from these grains since they crystallized. Individual monazite inclusions within allanite grains from both of these samples (Fig. 3) were also dated with the ion microprobe using the methods described in Harrison et al. (1995). Two allanite grains from the Atesina

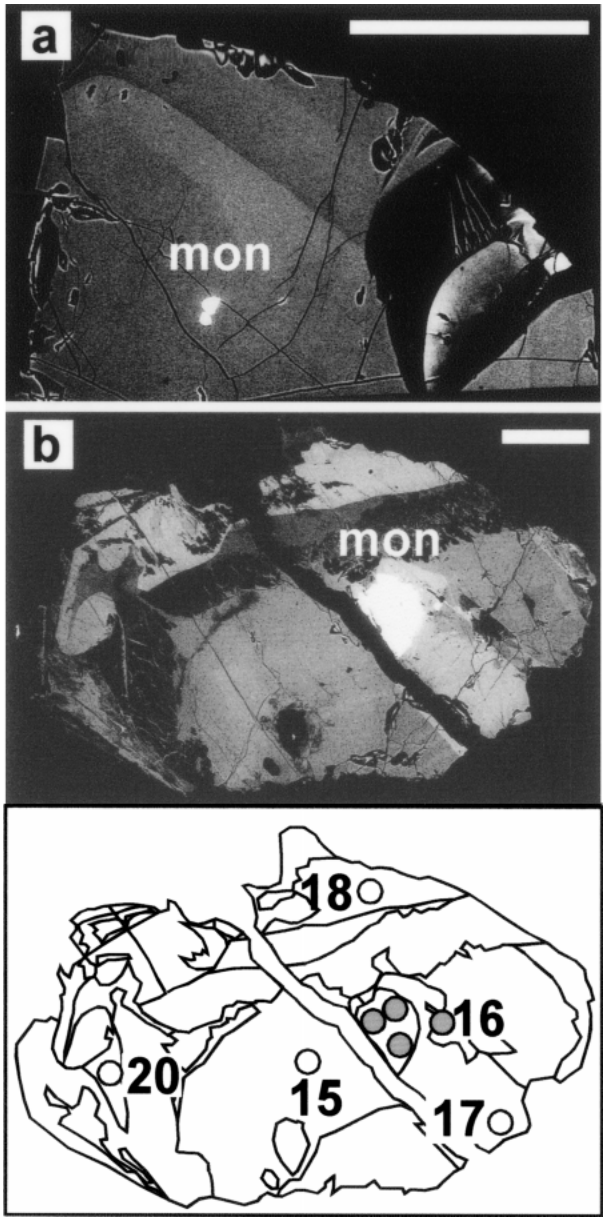

FIGURE 3. Backscattered electron images of (**a**) an Atesina Volcanic Complex allanite grain with a monazite inclusion and (**b**) a Cima d'Asta Pluton allanite grain (CAP2) with a monazite inclusion. The bright monazite is labeled "mon." The white scale bars are 100 µm. A map of the brightness zones is shown for CAP2, wherein the gray circles mark the locations of ion-microprobe analyses and open circles the locations of electron-microprobe analyses.

Volcanic Complex (AVC) rhyolite yielded an isotope dilution age of 276 ± 2 Ma (2σ; Barth et al. 1994a); we obtained a Th-Pb age for the monazite inclusion of 254 ± 26 Ma using the ion microprobe (2σ; assuming a common $^{208}Pb/^{204}Pb$ of 38.34). Although imprecise, this date is within the analytical uncertainties of the isotope-dilution age. A monazite inclusion within the Cima d'Asta plutonic (CAP) allanite analyzed using the ion microprobe yielded an age of 266 ± 12 Ma (2σ), consistent with the 276 ± 2 Ma age (2σ) determined for four single grains using the isotope-dilution method by Barth et al. (1994a). The third allanite is from the La Posta Pluton (LPP), eastern Peninsular Ranges batholith, southern California, which yielded a 94 ± 2 Ma (2σ) U-Pb zircon age (Walawender et al. 1990). We do not have a Th-Pb age on the coexisting allanite; however, because this rock cooled relatively rapidly following emplacement, we assume concordancy between the U-Pb zircon and Th-Pb allanite ages. Although zoning in the LPP allanite appears to be complex (Fig. 4), Clinkenbeard and Walawender (1989) reported that the pluton experienced little subsolidus deformation or alteration and thus provides an excellent opportunity to examine silicate minerals that retain their primary magmatic character.

Allanite compositions and zoning

Knowing the compositional variability within allanite grains analyzed with the ion microprobe is important because the compositionally dependent matrix effects can significantly alter the ionization efficiency of Th^+ and Pb^+ during sputtering. For example, Reed (1985) analyzed the REE content of allanite grains with the ion microprobe and determined a higher REE-oxide/element secondary-ion intensity ratio in allanite than in a standard REE-bearing glass (Drake and Weill 1972). This difference was attributed to a matrix effect, and Reed (1985) concluded that a compositionally characterized allanite rather than a synthetic glass should be used as an allanite standard. Thus to evaluate the role allanite composition plays in ion-microprobe analyses, we require detailed compositional information about the standard and unknown grains.

Allanite grains were analyzed using the JEOL electron microprobe at the Smithsonian Institution's National Museum of Natural History, operating at an accelerating potential of 15 kV and a probe current of 3.1×10^{-8} A. Corning synthetic standard glasses were used for Th (W glass) and U (X glass), and synthetic phosphates from Jarosewich and Boatner (1991) for Y and LREE. As each REE produces at least 12 X-ray lines in the L spectrum, finding interference-free regions for background measurements and peak intensities can be difficult (see Exley 1980; Williams 1996; Reed and Buckley 1998). For these allanite analyses, we used the LREE peak positions recommended by Exley (1980). Peak count times were 10 s with 5 s backgrounds for all elements in allanite, except Th, U, and P for which we used 30 s count times and 10 s backgrounds. Background and dead-time corrected apparent concentrations were further corrected for matrix effects by standard ZAF procedures. To check for systematic errors, four Drake and Weill (1972) glasses were analyzed after every six allanite analyses. Approximate detection limits and relative errors in the electron-microprobe determinations are given in Table 1.

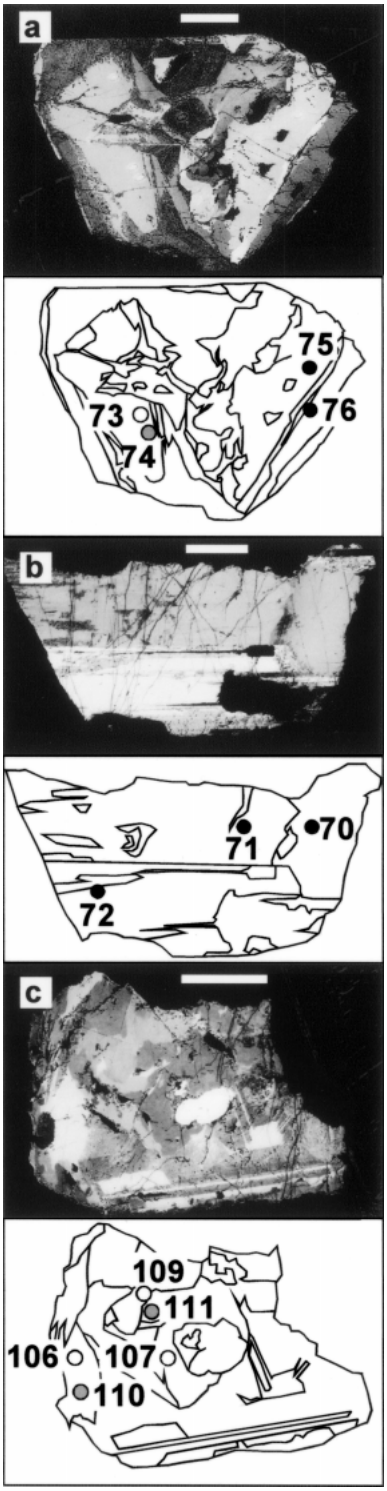

FIGURE 4. Backscattered electron images (upper) and maps of brightness zones (lower) of the La Posta Pluton allanite grains. Figure (**a**) is LPP2, (**b**) is LPP3, and (**c**) is LPP6. The open circles show the approximate locations of electron-microprobe analyses, the gray circles show the locations of ion-microprobe analyses, and the black dots show where both composition and age information were collected. The scale bars are 100 μm.

TABLE 1. Electron microprobe detection limits and approximate relative errors due to counting statistics (1σ)

	Detection limit (ppm)	Relative error (%)
Si	134	0.3
Al	99	0.4
Mg	88	2.8
Fe	335	1.1
Mn	269	5.4
Ca	130	0.7
Y	187	11
Th	2055	11
Ti	393	7.0
La	436	3.6
Ce	473	2.2
Nd	419	2.0
Pr	861	11
Sm	495	10
Gd	547	15
U	324	10

BSE images and electron-microprobe analyses reveal zoning in LREE, Fe, Th, and U within individual grains (see Figs. 3–6; and Tables 2–4). For all electron-microprobe analyses reported in this paper, the Fe^{2+}/Fe^{3+} was determined using the computer program LAG (Dollase and Newman 1984) on the basis of 8 cations and 12.5 oxygen atoms. Analyses of allanite from the La Posta Pluton indicate that the grains may exhibit some substitution of Al for Si. The BSE images show areas of single grains that appear to be cryptically altered. Areas on the grains that yielded compositional information inconsistent with allanite's mineral formula may have been altered by radiation damage, fluid-mineral interaction, or subsolidus reactions with adjacent phases; such areas were avoided during in-situ ion-microprobe analysis.

RESULTS

Electron microprobe analyses

The FeO contents of allanite grains vary from 15.7 to 17.6 wt% for the AVC, 9.2 to 13.9 wt% for the CAP, and 7.9 to 12.3 wt% for the LPP. Overall, Ce was the most abundant LREE in

TABLE 2. Compositions of allanites from La Posta Pluton (LPP)

spot*	LPP2			LPP3			LPP6		
	73	75	76	70	71	72	106	107	109
SiO_2	33.5	33.6	34.0	34.0	33.1	32.4	32.7	33.8	32.6
Al_2O_3	21.7	21.3	23.1	22.0	21.3	19.8	17.5	21.4	19.3
MgO	0.51	0.65	0.42	0.51	0.63	0.78	1.31	0.69	0.80
FeO†	6.1	7.0	4.3	7.2	7.0	10.0	10.4	7.4	7.6
Fe_2O_3†	4.0	3.2	5.7	3.0	3.0	0.7	2.2	2.9	3.7
MnO	0.43	0.43	0.46	0.47	0.38	1.20	0.41	0.36	0.33
CaO	15.0	14.8	17.0	14.7	14.4	10.5	11.2	14.6	13.7
Y_2O_3	0.23	0.18	0.51	0.24	0.22	0.50	0.05	0.13	0.06
ThO_2	0.2	0.6	0.2	0.2	0.9	0.4	1.0	0.4	1.2
TiO_2	–‡	0.4	0.2	0.2	0.4	0.2	0.8	0.4	0.9
La_2O_3	4.2	4.4	1.7	3.5	4.3	4.6	6.7	5.3	5.3
Ce_2O_3	8.5	9.0	6.0	8.2	8.7	11.3	12.0	9.9	9.1
Pr_2O_3	1.2	1.1	0.8	0.9	1.0	1.2	1.1	0.7	0.7
Nd_2O_3	3.1	3.2	3.9	3.7	3.3	4.7	2.9	2.3	2.3
Sm_2O_3	0.38	0.38	0.95	0.40	0.41	0.53	0.16	0.15	0.23
Gd_2O_3	0.88	1.20	1.24	1.16	1.09	1.57	1.34	1.05	1.20
UO_2	–	0.2	0.3	0.2	0.1	0.1	–	0.1	–
Total	100.0	101.6	100.9	100.5	100.3	100.4	101.8	101.7	99.1
				Formula proportions of cations					
Si	2.94	2.94	2.89	2.96	2.93	2.98	2.99	2.95	2.95
Al	2.25	2.20	2.32	2.26	2.23	2.14	1.89	2.20	2.06
Mg	0.07	0.08	0.05	0.07	0.08	0.11	0.18	0.09	0.11
Fe^{2+}	0.45	0.52	0.31	0.52	0.52	0.77	0.79	0.54	0.58
Fe^{3+}	0.26	0.21	0.37	0.19	0.20	0.05	0.15	0.19	0.25
Mn	0.03	0.03	0.03	0.03	0.03	0.09	0.03	0.03	0.03
Ca	1.42	1.38	1.55	1.38	1.37	1.04	1.10	1.37	1.33
Y	0.01	0.01	0.02	0.01	0.01	0.02	<0.01	0.01	<0.01
Th	<0.01	0.01	<0.01	<0.01	0.02	0.01	0.02	0.01	0.03
Ti	<0.01	0.02	0.01	0.01	0.03	0.01	0.06	0.03	0.06
La	0.13	0.14	0.05	0.11	0.14	0.15	0.23	0.17	0.18
Ce	0.27	0.29	0.19	0.26	0.28	0.38	0.40	0.32	0.30
Nd	0.10	0.10	0.12	0.12	0.10	0.15	0.09	0.07	0.07
Pr	0.03	0.02	0.02	0.02	0.02	0.03	0.02	0.01	0.02
Sm	0.01	0.01	0.03	0.01	0.01	0.02	0.01	<0.01	0.01
Gd	0.03	0.03	0.03	0.03	0.03	0.05	0.04	0.03	0.04
U	<0.01	<0.01	<0.01	<0.01	<0.01	<0.01	<0.01	<0.01	<0.01
A-site	2.00	2.00	2.02	1.95	1.99	1.85	1.92	1.99	1.97
M-site	3.06	3.07	3.09	3.10	3.08	3.17	3.10	3.07	3.08

* See Figure 4 for spot locations.
† For electron microprobe analyses reported in this paper, Fe^{2+}/Fe^{3+} was determined using the computer program LAG (Dollase and Newman 1984) on the basis of 8 cations and 12.5 oxygen atoms.
‡ "–", analyzed but not detected.

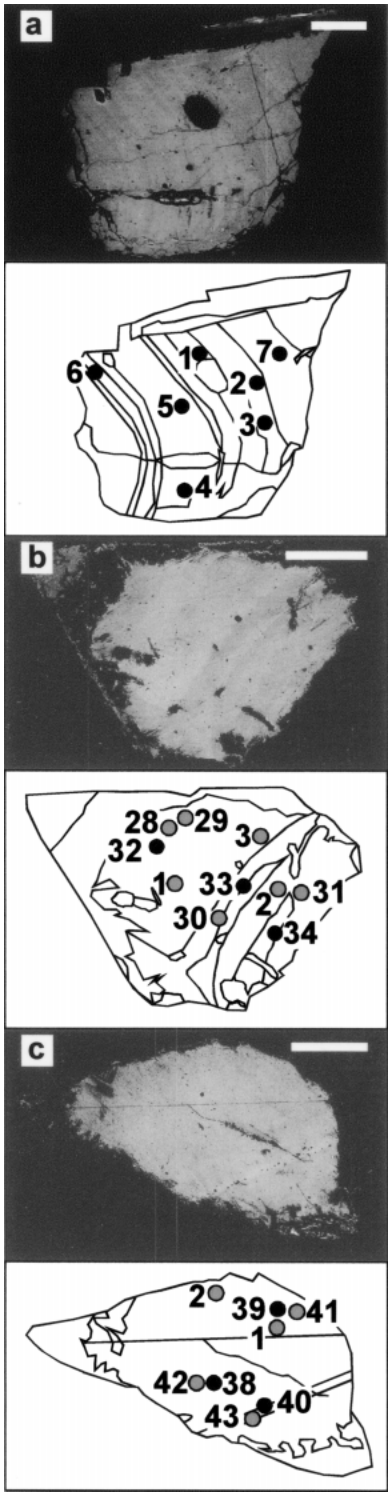

FIGURE 5. Backscattered electron images (upper) and maps of brightness zones (lower) of the Cima d'Asta Pluton allanite grains. Figure (**a**) is CAP1 (**b**) is CAP3 and (**c**) CAP 4. The numbered spots in the brightness zones follow the same criteria outlined in the caption for Figure 4. The scale bars are 100 μm.

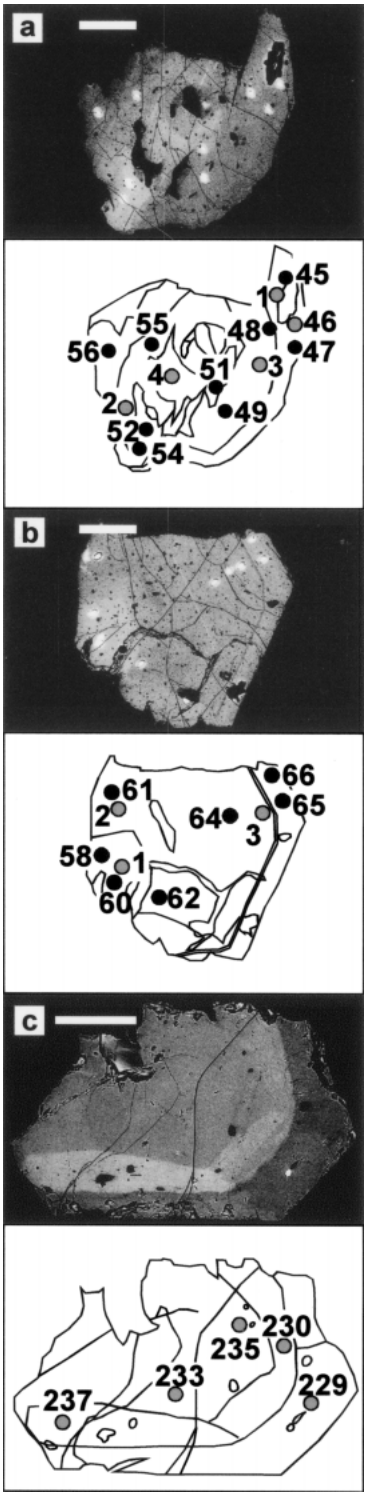

FIGURE 6. Backscattered electron images (upper) and maps of brightness zones (lower) of the Atesina Volcanic Complex allanite grains. Figure (**a**) is AVC5 (**b**) is AVC6 and (**c**) is AVC8. The numbered spots in the brightness zones follow the same criteria outlined in the caption for Figure 4. The scale bars are 100 μm.

TABLE 3. Compositions of allanites from the Cima d'Asta Pluton (CAP)

spot*	CAP1							CAP2				CAP3			CAP4		
	1	2	3	4	5	6	7	15	17	18	19	32	33	34	38	39	40
SiO_2	31.9	32.1	31.9	31.8	31.8	31.5	31.9	31.8	32.0	31.5	31.8	31.5	31.8	31.7	31.7	31.8	31.4
Al_2O_3	16.2	16.5	16.6	16.4	16.6	16.0	16.3	16.4	16.2	16.4	16.2	16.4	16.9	16.9	16.8	16.9	16.4
MgO	1.01	1.01	1.04	1.01	0.99	1.07	1.00	1.05	0.83	0.82	0.93	0.95	0.98	1.01	0.93	0.98	0.95
FeO†	11.3	11.4	11.2	11.4	11.7	10.8	11.0	10.9	12.2	11.5	11.0	11.4	11.7	11.9	11.9	11.7	11.8
Fe_2O_3†	2.0	1.7	2.0	2.1	1.5	2.7	2.3	3.0	1.7	2.8	2.3	1.4	1.5	1.0	1.1	0.9	1.7
MnO	0.30	0.27	0.27	0.21	0.21	0.26	0.44	0.28	0.67	0.55	0.26	0.48	0.36	0.48	0.44	0.39	0.53
CaO	10.3	10.3	10.4	10.3	10.1	10.3	10.3	10.5	9.7	9.7	10.6	9.7	9.8	9.4	9.6	9.9	9.3
Y_2O_3	0.22	0.28	0.22	0.22	0.22	0.24	0.27	0.19	0.65	0.77	0.28	0.28	0.23	0.17	0.27	0.23	0.17
ThO_2	0.9	1.0	1.0	1.3	1.0	1.1	1.2	1.1	1.4	1.1	1.3	1.4	0.9	1.0	1.4	1.5	0.8
TiO_2	0.7	0.5	0.7	0.6	0.7	0.6	0.6	0.6	0.5	0.4	0.7	0.8	0.7	0.7	0.6	0.8	0.7
La_2O_3	5.4	5.8	5.3	5.4	6.3	6.1	5.8	6.2	5.1	4.9	5.8	5.8	6.2	6.3	6.3	5.9	6.1
Ce_2O_3	12.3	12.7	12.8	12.8	13.4	11.2	10.2	10.9	11.0	11.2	11.9	11.7	12.7	12.6	12.3	12.9	13.1
Pr_2O_3	1.2	1.3	1.1	1.1	1.3	1.1	1.3	1.1	1.3	1.1	1.0	0.8	1.2	1.1	1.3	1.4	1.3
Nd_2O_3	4.0	4.0	4.1	4.3	4.3	4.4	4.2	3.9	5.2	4.9	3.9	4.2	4.2	4.3	4.3	4.2	4.2
Sm_2O_3	0.44	0.20	0.23	0.24	0.22	0.43	0.32	0.44	0.83	0.78	0.42	0.40	0.31	0.30	0.42	0.28	0.35
Gd_2O_3	1.64	1.61	1.55	1.64	1.66	1.61	1.69	1.60	1.66	1.72	1.50	0.35	0.32	0.50	0.13	0.24	0.33
UO_2	0.03	0.01	0.09	–‡	0.01	0.05	–	–	0.04	0.04	–						
P_2O_5	0.03	0.01	0.01	0.01	0.03	0.02	0.02	0.02	0.03	–	–						
Total	99.9	100.8	100.3	100.9	101.9	99.5	98.8	99.9	101.1	100.1	99.9	97.7	99.7	99.4	99.6	100.0	99.1
Formula proportions of cations																	
Si	3.02	3.02	3.00	3.00	2.99	3.00	3.03	3.00	3.02	2.99	3.01	3.03	3.01	3.02	3.01	3.01	3.01
Al	1.80	1.84	1.85	1.82	1.84	1.80	1.83	1.82	1.80	1.84	1.81	1.86	1.88	1.89	1.89	1.88	1.85
Mg	0.14	0.14	0.15	0.14	0.14	0.15	0.14	0.15	0.12	0.12	0.13	0.14	0.14	0.14	0.13	0.14	0.14
Fe^{2+}	0.90	0.89	0.88	0.90	0.92	0.86	0.88	0.86	0.96	0.91	0.87	0.92	0.93	0.94	0.94	0.93	0.95
Fe^{3+}	0.14	0.12	0.14	0.15	0.11	0.19	0.16	0.21	0.12	0.20	0.16	0.10	0.10	0.07	0.08	0.07	0.12
Mn	0.02	0.02	0.02	0.02	0.02	0.02	0.04	0.02	0.05	0.04	0.02	0.04	0.03	0.04	0.04	0.03	0.04
Ca	1.05	1.04	1.05	1.04	1.02	1.05	1.05	1.06	0.98	0.98	1.08	1.00	0.99	0.96	0.98	1.00	0.95
Y	0.01	0.01	0.01	0.01	0.01	0.01	0.01	0.01	0.03	0.04	0.01	0.01	0.01	0.01	0.01	0.01	0.01
Th	0.02	0.02	0.02	0.03	0.02	0.02	0.03	0.02	0.03	0.02	0.03	0.03	0.02	0.02	0.03	0.03	0.02
Ti	0.05	0.04	0.05	0.04	0.05	0.05	0.04	0.04	0.04	0.03	0.05	0.05	0.05	0.05	0.05	0.05	0.05
La	0.19	0.20	0.18	0.19	0.22	0.21	0.20	0.21	0.18	0.17	0.20	0.21	0.22	0.22	0.22	0.21	0.21
Ce	0.42	0.44	0.44	0.44	0.46	0.39	0.35	0.38	0.38	0.39	0.41	0.41	0.44	0.44	0.43	0.45	0.46
Nd	0.13	0.14	0.14	0.15	0.14	0.15	0.14	0.13	0.17	0.17	0.13	0.02	0.03	0.03	0.03	0.03	0.03
Pr	0.03	0.03	0.02	0.03	0.03	0.03	0.03	0.02	0.03	0.03	0.02	0.15	0.14	0.15	0.15	0.14	0.15
Sm	0.01	0.01	0.01	0.01	0.01	0.01	0.01	0.01	0.03	0.03	0.01	0.01	0.01	0.01	0.01	0.01	0.01
Gd	0.05	0.05	0.05	0.05	0.05	0.05	0.05	0.05	0.05	0.05	0.05	0.01	0.01	0.02	<0.01	0.01	0.01
U	<0.01	<0.01	<0.01	<0.01	<0.01	<0.01	<0.01	<0.01	<0.01	<0.01	<0.01						
P	<0.01	<0.01	<0.01	<0.01	<0.01	<0.01	<0.01	<0.01	<0.01	<0.01	<0.01						
A-site	1.92	1.94	1.92	1.94	1.96	1.93	1.88	1.90	1.89	1.88	1.95	1.85	1.87	1.85	1.87	1.89	1.85
M-site	3.06	3.05	3.08	3.08	3.06	3.07	3.09	3.10	3.10	3.14	3.04	3.11	3.12	3.14	3.12	3.10	3.15

* See Figures 3 and 5 for spot locations.
† For electron microprobe analyses reported in this paper, Fe^{2+}/Fe^{3+} was determined using the computer program LAG (Dollase and Newman 1984) on the basis of 8 cations and 12.5 oxygen atoms.
‡ "–", analyzed but not detected.

the allanite grains analyzed in this study. The Ce_2O_3 contents vary from 11.7 to 13.4 wt% for AVC, 9.0 to 13.4 wt% for the CAP, and 6.0 to 12.0 wt% for the LPP. The relative order of LREE content in these allanite grains is Ce > La > Nd > Pr > Gd > Sm and a chondrite-normalized plot shows these allanite grains to be LREE enriched (Fig. 7). The chordrite-normalized patterns in Figure 7 indicate that some areas within individual grains are enriched in Sm relative to Gd. The intent of this plot is to discern any striking differences in LREE behavior between the grains used as standards and those treated as unknowns. The LREE patterns of the standard allanite grains are similar to those analyzed as unknowns, and to some LREE patterns in allanite reported from other locations (see Lee and Barston 1967; Exley 1980; Ward et al. 1992).

More than 150 analyses of 26 allanite grains are compared to those reported in the literature by assigning elements to sites and displaying the results in terms of the geological setting (Fig. 8). The elements assigned to the A-sites are REE, Ca, Sr, Th, and U, whereas Fe, Al, Mg, Cr, Mn, and Ti are assigned to the M-sites. Our analyses include allanite grains from pelites and gneisses from central Nepal, granulite facies rocks near Cauchon Lake, Manitoba, the Pacoima Canyon pegmatite in southern California, Long Valley rhyolite and domes in central California, and the standards used in this study. Our data in this plot have Si between 2.97 and 3.01 atoms per formula unit (apfu) and oxide totals between 97 and 100 wt%. By plotting the A-site vs. M-site occupancy, we find a consistent deficiency in the A-site and excess in the M-site (Fig. 8). The lines in Figure 8 show how the data would plot if the A-site deficiency was balanced by an M-site excess, as would be the case if some cation (a portion there of) was assigned to the M-site instead of the A-site. Peterson and MacFarlane (1993) interpreted the A-site deficiency to result from a vacancy substitution of the form: $3Ca^{2+} \leftrightarrow 2REE^{3+} + \square$. Most of the data in Figure 8, however, lie along the line, indicating A-site deficiency = M-site excess. A simple explanation is that some Fe^{2+} has been incorporated into the A sites, substituting for Ca^{2+}. The possible presence of Fe^{2+} in the A-sites has implications for the calculation of oxygen fugacities from allanite compositional data (e.g., Petrík et al. 1995).

TABLE 4. Compositions of allanite from the Atesina Volcanic Complex (AVC)

spot*	AVC5								AVC6							
	45	47	48	49	51	52	54	55	56	58	60	61	62	64	65	66
SiO_2	30.5	30.9	31.0	31.0	30.9	31.0	30.8	31.0	31.3	30.7	30.9	30.8	31.2	31.1	31.0	31.1
Al_2O_3	14.0	14.1	14.2	14.1	14.0	13.3	13.2	14.2	14.0	13.9	13.7	13.8	14.4	14.3	14.4	14.4
MgO	0.63	0.64	0.64	0.65	0.41	0.41	0.40	0.41	0.59	0.49	0.58	0.55	0.51	0.43	0.53	0.41
FeO	13.3	13.2	14.0	13.9	14.4	14.9	15.4	14.3	14.2	14.2	14.3	13.7	13.9	13.6	13.8	14.1
Fe_2O_3	3.5	3.0	2.2	2.0	3.0	2.5	2.4	2.9	2.6	2.5	1.9	3.0	2.5	2.5	2.5	2.3
MnO	0.36	0.33	0.38	0.38	0.63	0.63	0.57	0.71	0.35	0.31	0.43	0.43	0.38	0.41	0.43	0.65
CaO	8.6	8.8	8.6	8.6	8.1	7.9	7.7	8.1	8.6	8.3	8.3	8.6	8.6	8.8	8.5	8.1
Y_2O_3	0.23	0.37	0.30	0.38	0.67	0.84	0.96	0.62	0.42	0.49	0.57	0.45	0.44	0.51	0.49	0.65
ThO_2	1.2	0.9	1.4	1.4	1.0	1.1	1.6	0.8	0.9	1.5	1.8	1.2	0.9	0.9	1.1	0.9
TiO_2	1.4	1.2	1.3	1.3	1.0	1.0	1.1	0.8	1.2	1.0	1.2	1.4	1.0	0.9	0.9	0.8
La_2O_3	5.4	5.7	5.4	6.3	5.1	5.9	5.6	5.4	6.1	5.5	5.2	5.2	5.4	5.4	5.8	4.5
Ce_2O_3	12.8	12.7	12.8	12.7	12.5	12.7	13.4	13.3	12.6	13.2	12.8	12.5	12.8	12.8	13.3	12.2
Pr_2O_3	1.2	1.0	1.6	1.5	1.9	1.7	1.8	1.7	1.6	1.3	1.5	1.2	1.2	1.3	1.3	1.1
Nd_2O_3	4.8	4.8	4.8	4.3	5.1	5.0	4.9	5.1	4.5	4.7	4.7	4.4	4.8	4.8	4.7	5.2
Sm_2O_3	0.46	0.55	0.55	0.54	0.73	0.81	0.77	0.78	0.52	0.59	0.55	0.51	0.63	0.64	0.52	1.02
Gd_2O_3	0.30	0.10	0.49	0.50	0.53	0.52	0.66	0.49	0.47	0.43	0.54	0.33	0.32	0.53	0.23	0.67
Total	98.4	98.3	99.7	99.6	100.0	100.3	101.3	100.5	99.9	99.2	98.8	98.0	99.0	98.9	99.4	98.1
Formula proportions of cations																
Si	2.99	3.02	3.02	3.03	3.02	3.04	3.02	3.02	3.03	3.03	3.05	3.03	3.04	3.04	3.03	3.06
Al	1.62	1.63	1.63	1.62	1.61	1.54	1.53	1.62	1.60	1.61	1.59	1.60	1.65	1.65	1.65	1.67
Mg	0.09	0.09	0.09	0.09	0.06	0.06	0.06	0.06	0.08	0.07	0.09	0.08	0.07	0.06	0.08	0.06
Fe^{2+}	1.09	1.08	1.14	1.14	1.17	1.22	1.26	1.16	1.15	1.17	1.18	1.13	1.13	1.11	1.12	1.16
Fe^{3}†	0.26	0.22	0.16	0.15	0.22	0.19	0.18	0.22	0.19	0.18	0.14	0.22	0.18	0.19	0.18	0.17
Mn	0.03	0.03	0.03	0.03	0.05	0.05	0.05	0.06	0.03	0.03	0.04	0.04	0.03	0.03	0.04	0.05
Ca	0.90	0.92	0.90	0.90	0.85	0.83	0.81	0.84	0.89	0.87	0.87	0.90	0.90	0.92	0.89	0.85
Y	0.01	0.02	0.02	0.02	0.04	0.04	0.05	0.03	0.02	0.03	0.03	0.02	0.02	0.03	0.03	0.03
Th	0.03	0.02	0.03	0.03	0.02	0.03	0.04	0.02	0.02	0.03	0.04	0.03	0.02	0.02	0.03	0.02
Ti	0.10	0.09	0.10	0.09	0.07	0.08	0.08	0.06	0.09	0.07	0.09	0.10	0.08	0.07	0.06	0.06
La	0.20	0.20	0.19	0.23	0.19	0.21	0.20	0.19	0.22	0.20	0.19	0.19	0.19	0.19	0.21	0.16
Ce	0.46	0.45	0.46	0.45	0.45	0.46	0.48	0.47	0.45	0.48	0.46	0.45	0.46	0.46	0.47	0.44
Nd	0.03	0.02	0.04	0.04	0.05	0.04	0.04	0.04	0.04	0.03	0.04	0.03	0.03	0.03	0.03	0.03
Pr	0.17	0.17	0.17	0.15	0.18	0.18	0.17	0.18	0.16	0.16	0.17	0.16	0.17	0.17	0.16	0.18
Sm	0.02	0.02	0.02	0.02	0.02	0.03	0.03	0.03	0.02	0.02	0.02	0.02	0.02	0.02	0.02	0.03
Gd	0.01	<0.01	0.02	0.02	0.02	0.02	0.02	0.02	0.02	0.01	0.02	0.01	0.01	0.02	0.01	0.02
A-site	1.82	1.83	1.83	1.85	1.80	1.83	1.84	1.82	1.82	1.84	1.83	1.80	1.82	1.85	1.84	1.77
M-site	3.19	3.14	3.15	3.12	3.18	3.14	3.16	3.17	3.15	3.14	3.12	3.17	3.15	3.11	3.13	3.17

*See Figure 6 for spot locations.

† For electron microprobe analyses reported in this paper, Fe^{2+}/Fe^{3+} was determined using the computer program LAG (Dollase and Newman 1984) on the basis of 8 cations and 12.5 oxygen atoms.

Ion microprobe analyses

For dating of monazite using the Th-Pb ion-microprobe method, a linear relationship between $^{208}Pb^*/Th^+$ vs. ThO_2^+/Th^+ is typically observed for multiple spot analyses on grains used as age standards (Harrison et al. 1995, 1999). Because the CAP and AVC allanite grains are of similar age [276 ± 2 Ma (2σ), Barth et al. 1994a], by analogy to monazite, we expected to observe the same linear relationship for the allanite. However, the ThO_2^+ sputtering yield is enhanced in allanite from the AVC relative to the allanite from CAP (Fig. 9). Using the conventional 2-D calibration, we could not reproduce the age of AVC allanite using the CAP allanite as a standard with a defined 276 Ma age (Table 5). Thirteen ion-microprobe spots on two CAP allanite grains yielded a poor linear correlation coefficient of 0.41 between $^{208}Pb^*/Th^+$ vs. ThO_2^+/Th^+. Using this calibration line, seventeen ion-microprobe spots on two of the AVC allanite grains yielded a significantly younger apparent age of 137 ± 20 Ma (2σ) than that reported by Barth et al. (1994a).

Electron-microprobe analyses show that the two allanite grains differ by 4–7 wt% FeO(Tables 3 and 4). Because Fe is a major constituent of allanite and because previous studies have documented matrix effects associated with Fe-bearing minerals (Shimizu et al. 1978; Ray and Hart 1982; Havette 1985; Shimizu and LeRoex 1986), we used Fe as a proxy to examine the relative ionization efficiencies. On a plot FeO^+/SiO^+ vs. ThO_2^+/Th^+, spots on allanite grains from five different localities and having different Fe concentrations yield a roughly linear relationship (Fig. 10).

By adding Fe content as a third dimension to the typical calibration plot, we obtained an internally consistent set of ion microprobe ages that agree within uncertainty with results from single-grain, isotope-dilution measurements. Initially, we used the Fe content measured with the electron microprobe at the spot from which the isotopic data were obtained. For the data reported in this paper, we obtained an ion-microprobe measurement of the FeO^+/SiO^+ ratio on the same spot used for the Pb and Th analyses.

When plotted in the three-dimensional space described above, the CAP and AVC allanite grains lie on the same cali-

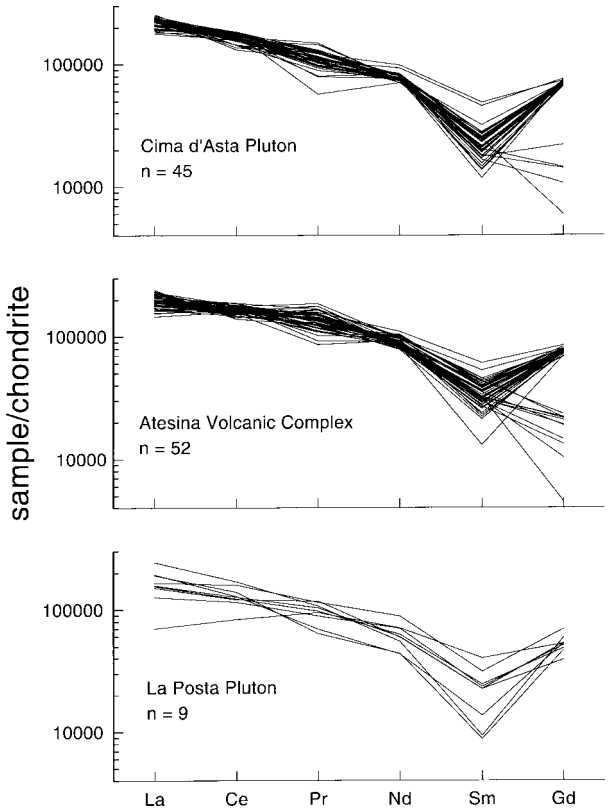

FIGURE 7. Chondrite normalized, light rare-earth element patterns for the Cima d'Asta Pluton, Atesina Volcanic Complex, and La Posta Pluton allanite grains [chondrite concentrations from Anders and Grevesse (1989)].

TABLE 5. Th-Pb ion-microprobe age results for the Atesina Volcanic Complex (AVC) allanite using the 2-D calibration method and the Cima d'Asta Pluton (CAP) allanite as the standard*

grain_spot†	Age (Ma)‡	%^{208}Pb*§	^{208}Pb*/Th$^+$‖	ThO$_2^+$/Th$^+$#
CAP3_28	289 (9)	95.3	0.01441 (0.00046)	2.010 (0.007)
CAP3_29	259 (6)	96.7	0.01291 (0.00030)	2.057 (0.007)
CAP3_30	288 (10)	96.3	0.01432 (0.00050)	1.985 (0.006)
CAP3_31	268 (9)	93.1	0.01334 (0.00043)	2.006 (0.008)
CAP3_32	260 (13)	97.1	0.01296 (0.00054)	2.177 (0.019)
CAP3_33	298 (7)	95.7	0.01485 (0.00035)	2.106 (0.008)
CAP3_34	291 (7)	94.6	0.01448 (0.00035)	2.121 (0.009)
CAP4_38	253 (7)	97.0	0.01258 (0.00036)	2.215 (0.008)
CAP4_39	302 (7)	96.0	0.01503 (0.00034)	2.098 (0.007)
CAP4_40	257 (9)	96.6	0.01281 (0.00045)	2.280 (0.010)
CAP4_41	282 (11)	94.5	0.01405 (0.00054)	1.978 (0.007)
CAP4_42	272 (8)	94.5	0.01356 (0.00039)	2.020 (0.008)
CAP4_43	237 (7)	92.6	0.01179 (0.00032)	2.150 (0.009)
AVC5_45	143 (10)	97.7	0.00711 (0.00051)	3.247 (0.015)
AVC5_46	128 (9)	94.9	0.00635 (0.00045)	3.212 (0.022)
AVC5_47	133 (10)	93.7	0.00659 (0.00047)	3.247(0.020)
AVC5_48	150 (11)	95.8	0.00745 (0.00054)	3.245 (0.029)
AVC5_49	139 (10)	95.1	0.00692 (0.00050)	3.291 (0.019)
AVC5_51	133 (10)	94.7	0.00662 (0.00049)	3.372 (0.022)
AVC5_52	148 (11)	95.7	0.00736 (0.00056)	3.585 (0.021)
AVC5_54	169 (13)	95.1	0.00841 (0.00062)	3.431 (0.018)
AVC5_55	152 (11)	93.8	0.00754 (0.00055)	3.312 (0.018)
AVC5_56	169 (12)	95.5	0.00838 (0.00060)	3.198 (0.019)
AVC6_58	128 (9)	97.7	0.00633 (0.00044)	3.123 (0.012)
AVC6_60	121 (8)	97.7	0.00602 (0.00039)	2.958 (0.009)
AVC6_61	123 (8)	98.2	0.00612 (0.00042)	3.066 (0.010)
AVC6_62	132 (9)	95.4	0.00652 (0.00043)	2.992 (0.011)
AVC6_64	119 (8)	94.9	0.00592 (0.00039)	2.933 (0.014)
AVC6_65	120 (8)	97.5	0.00593 (0.00038)	2.900 (0.013)
AVC6_66	116 (7)	96.6	0.00574 (0.00037)	2.896 (0.012)

* The age of the Atesina Volcanic Complex (AVC) allanite was calculated using the Cima d'Asta Pluton (CAP) allanite as the standard with a defined 276 Ma age [$(^{208}Pb^*/Th)_s = 1.37 \times 10^{-2}$]. See Figure 9 for the 2-D calibration plot and Table 8 for a summary of this age data.
† The nomenclature indicates the grain and spot, respectively, of the analyzed allanite. See Figures 5 and 6 for spot locations.
‡ The quantity in parenthesis is the 1σ error.
§ The %^{208}Pb* is the percent radiogenically-derived ^{208}Pb.
‖ Corrected sample ratio assuming (^{208}Pb/^{204}Pb) = 38.34 (Barth et al. 1994a).
Measured ratio in sample.

bration plane, whereas the LPP allanite grains are younger and define a separate, internally consistent calibration (Figs. 11, 12, 13; Tables 6, 7, 8, and 9). The plane may be described by the equation $^{208}Pb^*/Th^+ = A(FeO^+/SiO^+) + B(ThO_2^+/Th^+) + C$, where A, B, and C are constants derived by multivariate regression of several ion-microprobe spot analyses of the allanite age standard. The age of an unknown is given by $(\ln \{1 + [(^{208}Pb^*/Th)_s(^{208}Pb^*/Th^+)_{unk}] / [A(FeO^+/SiO^+) + B(ThO_2^+/Th^+) + C]\})/\lambda$, where $(^{208}Pb^*/Th)_s$ is the known ratio for the standard corrected for common Pb, $(^{208}Pb^*/Th^+)_{unk}$ is the ion-microprobe ratio corrected for common Pb for an allanite grain of unknown age, and λ is the decay constant of ^{232}Th in y^{-1}. If the system remained closed to Pb loss, a 276 Ma allanite grain should have $(^{208}Pb^*/Th)_s = 1.37 \times 10^{-2}$ and a 94 Ma allanite grain should have $(^{208}Pb^*/Th)_s = 4.66 \times 10^{-3}$.

Using the AVC allanite as the 276 Ma age standard (Table 6 and Fig. 11), an age of 288 ± 6 Ma (1σ) was determined for nine spots on three CAP allanite grains. If the 2-D calibration was used, the same spot analyses yield an older, more uncertain age of 324 ± 24 Ma (1σ). In Table 7 and Figure 12, we use the LPP allanite as the 94 Ma age standard to calculate the ages of the CAP and AVC allanite grains. Twelve spot analyses on three LPP allanite grains define the plane, which yielded 259 ± 14 Ma (1σ, 3 spots on 1 grain) for the AVC and 250 ± 14 Ma (1σ, 8 spots on 3 grains) for the CAP allanite samples. Although the ages show a wide range (i.e., from 180 ± 11 Ma to 299 ± 17 Ma for the CAP allanite in Table 7), the average age of all the results are within 2σ of the single-grain, isotope-dilution ages reported by Barth et al. (1994a).

Table 8 summarizes the ion-microprobe results from the CAP, AVC, and LPP allanite grains analyzed in this study. The CAP and AVC allanite grains produce a 3-D calibration curve from which we can calculate an age of 276 Ma with an accuracy of 2–5%, whereas the LPP allanite calibration curve yields an age of 94 Ma with an accuracy of 6–12%. The lower accuracy results from the LPP may either be related to the amount of $^{208}Pb^*$ [the AVC and CAP allanite grains are highly radiogenic (97 ± 2%) whereas the LPP allanite grains are somewhat less so (73 ± 15%)] or reflect additional matrix effects.

The data in Table 8 indicates that the 3-D calibration method

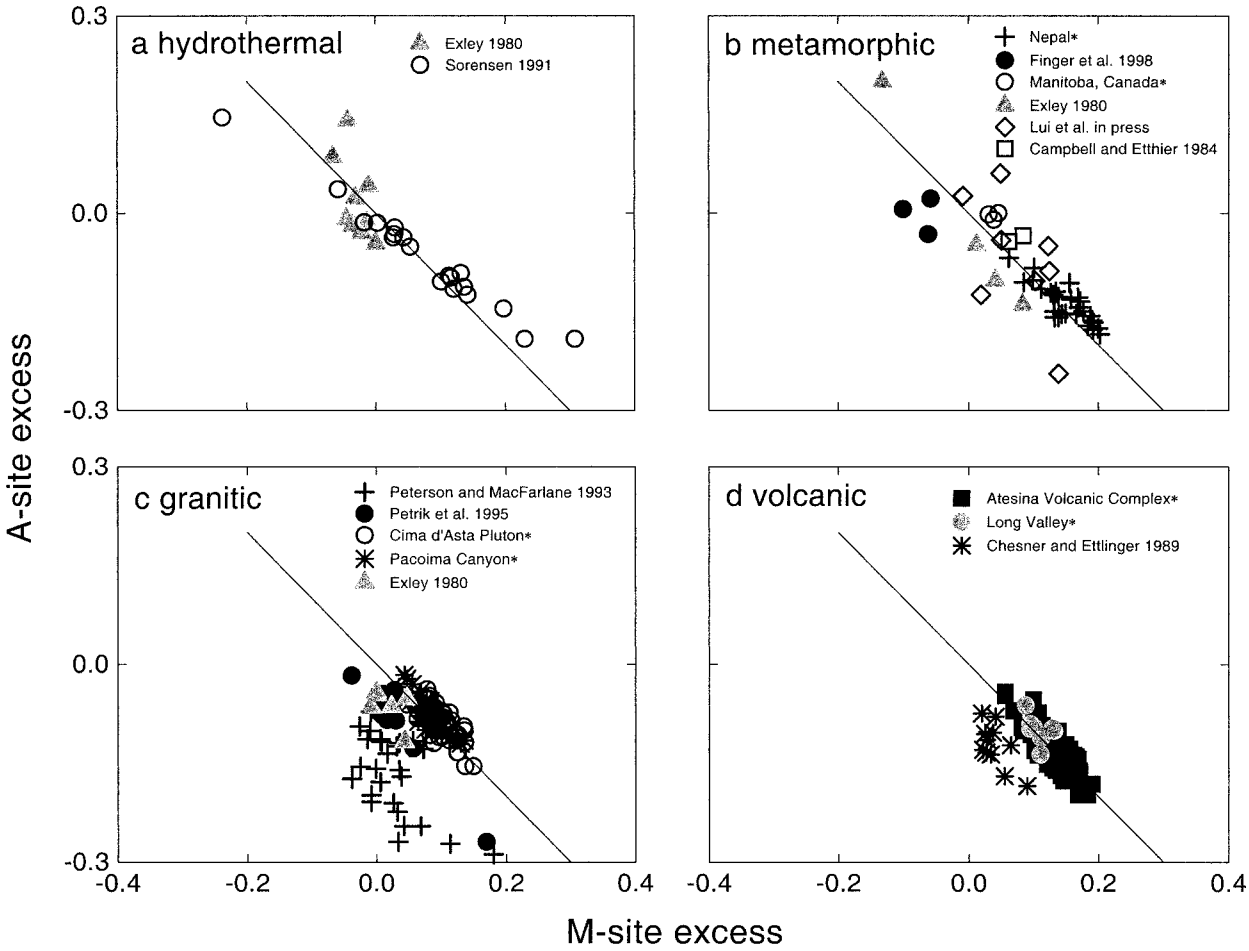

FIGURE 8. Plot of cation excess in the allanite M-site [= 3 – (Al + Mg + Fe + Ti + Cr + Mn)] vs. cation excess in the A-site [= 2 – (Ca + ΣREE + Sr + Th + U)]. The reference line corresponds to A-site excess = M-site deficiency (and vice-versa) in the electron-microprobe analyses. Data generated for this study are designated by asterisks. (**a**) Hydrothermal allanite from the Tertiary Igneous Complex, Isle of Skye, Scotland (Exley 1980) and from garnet amphibolite blocks, Catalina Schist, Southern California (Sorensen 1991). (**b**) Metamorphic allanite grains from a metagranite, Tauren Window, eastern Alps (Finger et al. 1998), from the Isle of Skye, Scotland (Exley 1980), from an ultrahigh-pressure metamorphic terrane, Dabie Shan, central China (Liu et al. in press), and from the Sullivan Orebody, British Columbia (Campbell and Etthier 1984). Our data include metamorphic allanite collected near the Main Central Thrust, Nepal Himalaya and from granulite facies rocks near Cauchon Lake, Manitoba, Canada. (**c**) Granitic allanite grains from the Grenville province, Southeastern Ontario (Peterson and MacFarlane 1993), from the Western Carpathians, Slovakia (Petrík et al. 1995), and from the Isle of Skye, Scotland (Exley 1980). Our data are from the Cima d'Asta granodiorite pluton, Italy, and from the Pacoima Canyon pegmatite, southern California. (**d**) Volcanic allanite grains from the Toba tuffs, Sumatra, Indonesia (Chesner and Ettlinger 1989). Our data are from the Atesina Volcanic Complex rhyolite, Italy, and from Long Valley rhyolite and domes, California.

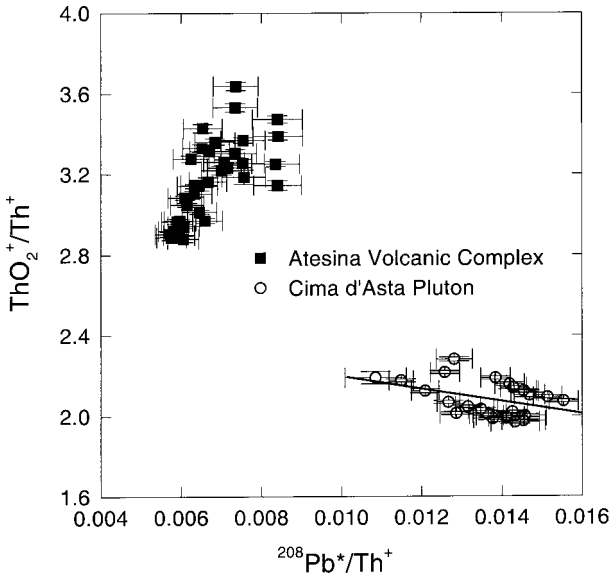

FIGURE 9. Two-dimensional calibration plot of $^{208}Pb^*/Th^+$ vs. ThO_2^+/Th^+ for the Atesina Volcanic Complex and Cima d'Asta Pluton allanite. See Tables 5 and 8 for numerical results.

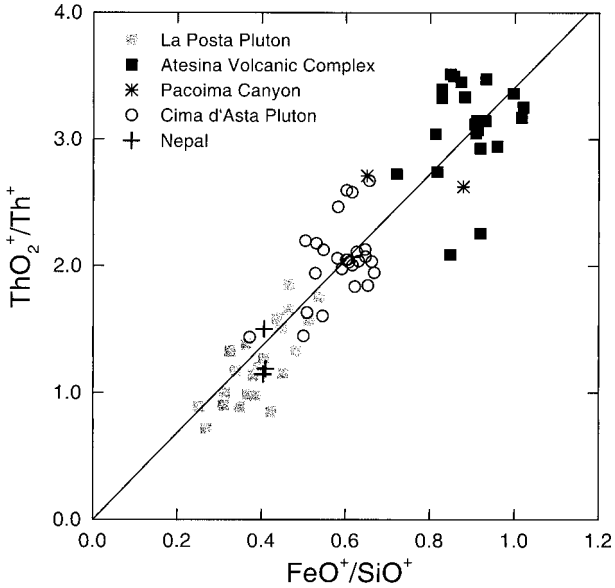

FIGURE 10. Plot of FeO^+/SiO^+ vs. ThO_2^+/Th^+ for allanite dated in this study. The isotopic data (n = 76 points) were taken from ion-microprobe spots on the allanite grains. The linear best-fit for the data satisfies the form: $ThO_2^+/Th^+ = A(FeO^+/SiO^+)$, where $A = 3.4 \pm 0.1$, the correlation coefficient is 0.92.

can significantly improve the precision and accuracy of age determinations for allanite grains with different Fe contents over the 2-D calibration method. In this study, the 3-D calibration method is applied to allanite grains with different Fe contents. If the allanite grains had similar Fe concentrations, the 2-D calibration of $^{208}Pb^*/Th^+$ vs. ThO_2^+/Th^+ has the potential for better results because the sputtering yield of Pb^+ and Th^+ from both standard and unknown would be affected the same way. The 3-D calibration method is intended for ion-microprobe analysis of allanite grains that differ by more than about 1 wt% FeO from the allanite standard. The matrix effects on the ionization efficiency of Pb^+ and Th^+ restrict the use of the 2-D calibration to compositionally well-characterized standards and unknowns that have essentially the same Fe content.

The accuracy of this method for Th-Pb analyses of allanite is less than that routinely expected from U-Th-Pb analyses of zircon or monazite and is probably due to the large compositional variability of allanite relative to these other two phases. Nevertheless, several important geological problems can be addressed using this dating method.

APPLICATION OF THE METHOD

The 3-D Th-Pb calibration method was applied to allanite grains from two different geological environments: metamorphic allanite from the footwall of a major thrust fault in central Nepal and allanite from the Pacoima Canyon pegmatite in southern California.

Garnet-bearing schist samples MA27 and MA33 were collected beneath the Main Central Thrust along the Marysandi River in central Nepal. The Main Central Thrust is one of the major tectonic structures in the nappe complex that formed as the result of the collision that telescoped the Indian margin (e.g., Le Fort 1996). The fault marks the break in slope of the present-day Himalayan mountain range and has accommodated several hundred kilometers of slip (Srivastava and Mitra 1994). There is no metamorphic break across the Main Central Thrust, and metamorphism within the footwall increases up section (i.e., is "inverted") toward the fault from zeolite to kyanite grade over a N-S distance of ~20 km (e.g., Colchen et al. 1986). The origin of the apparent inverted metamorphic sequence has been linked to slip along the Main Central Thrust (e.g., Le Fort 1996) and may have important implications for understanding heat flow adjacent to large thrust faults. In addition, thrusting along the fault has been proposed to occur simultaneously with extension within the range (e.g., Hodges et al. 1992). Knowing the slip history of the Main Central Thrust is important to deciphering the evolution of the Himalayan range, and significant gaps remain in our understanding of this orogen.

Geochronological studies show the hanging wall was deforming at ~22 Ma (e.g., Hodges et al. 1996). Th-Pb ion-microprobe analyses of monazite inclusions in garnet grains from rocks of the inverted metamorphic sequence indicate the footwall shear zone was active at ~6 Ma (e.g., Harrison et al. 1997). Petrographic observations of pelitic rocks indicate that monazite first appears in the garnet zone, whereas allanite is the principal host of LREE in chlorite- and biotite-zone rocks in the footwall of the thrust. To determine if the allanite grains record Late Miocene footwall recrystallization, we made ion-micro-

TABLE 6. Th-Pb ion-microprobe age results for the Cima d'Asta Pluton (CAP) allanite using the 3-D calibration method and the Atesina Volcanic Complex (AVC) allanite as the standard*

grain_spot†	Age (Ma)	%^{208}Pb*	FeO$^+$/SiO$^+$	^{208}Pb*/Th$^+$	ThO$_2^+$/Th$^+$
AVC5_1	277 (6)	99.1	0.912 (0.009)	0.44199 (0.00142)	3.072 (0.008)
AVC5_2	276 (7)	98.1	1.020 (0.019)	0.46705 (0.00234)	3.252 (0.011)
AVC5_3	278 (6)	98.9	0.908 (0.009)	0.43961 (0.00220)	3.050 (0.008)
AVC5_4	277 (6)	98.0	0.997 (0.008)	0.48706 (0.00259)	3.361 (0.012)
AVC6_1	270 (6)	98.9	0.910 (0.011)	0.44327 (0.00176)	3.145 (0.006)
AVC6_2	276 (7)	98.5	1.016 (0.020)	0.45192 (0.00206)	3.171 (0.009)
AVC6_3	280 (6)	99.1	0.906 (0.009)	0.45457 (0.00157)	3.120 (0.011)
AVC8_229	275 (5)	99.0	0.828 (0.004)	0.48540 (0.00126)	3.327 (0.010)
AVC8_230	271 (5)	98.9	0.873 (0.003)	0.49875 (0.00131)	3.452 (0.009)
AVC8_233	275 (5)	98.8	0.828 (0.004)	0.49815 (0.00209)	3.396 (0.013)
AVC8_235	284 (5)	98.8	0.848 (0.004)	0.53362 (0.00149)	3.514 (0.008)
AVC8_237	274 (5)	99.2	0.856 (0.003)	0.51138 (0.00187)	3.498 (0.013)
CAP3_1	297 (6)	98.9	0.604 (0.003)	0.29789 (0.00108)	2.048 (0.007)
CAP3_2	299 (6)	99.0	0.631 (0.003)	0.29641 (0.00114)	2.037 (0.005)
CAP3_3	301 (6)	99.1	0.662 (0.005)	0.29651 (0.00094)	2.033 (0.008)
CAP4_1	300 (5)	99.0	0.601 (0.001)	0.30126 (0.00100)	2.046 (0.004)
CAP4_2	299 (7)	99.1	0.608 (0.008)	0.29661 (0.00111)	2.029 (0.005)
CAP8_218	275 (5)	99.3	0.656 (0.004)	0.38062 (0.00138)	2.675 (0.009)
CAP8_219	259 (6)	99.0	0.582 (0.010)	0.32858 (0.00079)	2.468 (0.008)
CAP8_221	279 (5)	99.3	0.615 (0.003)	0.37228 (0.00139)	2.584 (0.009)
CAP8_222	281 (6)	98.3	0.602 (0.005)	0.37846 (0.00198)	2.599 (0.014)

* The age of the Cima d'Asta Pluton (CAP) allanite was calculated using the Atesina Volcanic Complex (AVC) allanite as the standard with a defined 276 Ma age [$(^{208}Pb^*/Th)_s = 1.37 \times 10^{-2}$]. See Figure 11 for the 3-D calibration plot and Table 8 for a summary of this age data.
† The nomenclature indicates the grain and spot, respectively, of the analyzed allanite. See Figures 5 and 6 for spot locations.

TABLE 7. Th-Pb ion-microprobe age results for the Cima d'Asta Pluton (CAP) and Atesina Volcanic Complex (AVC) allanite using the 3-D calibration method and the La Posta Pluton (LPP) allanite as the standard*

grain_spot†	Age (Ma)	%^{208}Pb*	FeO$^+$/SiO$^+$	^{208}Pb*/Th$^+$	ThO$_2^+$/Th$^+$
LPP2_73	103 (8)	73.0	0.385 (0.004)	0.02391 (0.00142)	0.975 (0.006)
LPP2_74	99 (8)	71.0	0.347 (0.001)	0.02009 (0.00121)	0.886 (0.006)
LPP2_75	88 (6)	74.8	0.309 (0.001)	0.01797 (0.00092)	0.899 (0.005)
LPP2_76	92 (16)	46.2	0.268 (0.005)	0.01296 (0.00211)	0.711 (0.007)
LPP2_77	95 (10)	50.3	0.313 (0.003)	0.02262 (0.00214)	0.999 (0.007)
LPP3_70	78 (9)	60.2	0.423 (0.007)	0.01503 (0.00156)	0.848 (0.006)
LPP3_71	94 (9)	75.4	0.251 (0.011)	0.01873 (0.00139)	0.889 (0.007)
LPP3_72	97 (6)	79.3	0.481 (0.005)	0.03425 (0.00135)	1.329 (0.008)
LPP6_106	92 (5)	91.5	0.447 (0.004)	0.03793 (0.00081)	1.511 (0.008)
LPP6_109	97 (6)	86.0	0.450 (0.009)	0.02839 (0.00081)	1.153 (0.006)
LPP6_110	92 (6)	91.1	0.437 (0.010)	0.03995 (0.00090)	1.585 (0.008)
LPP6_111	100 (7)	82.2	0.367 (0.008)	0.02354 (0.00081)	0.983 (0.005)
CAP5_1	258 (14)	98.2	0.508 (0.004)	0.11767 (0.00033)	1.631 (0.003)
CAP5_2	180 (11)	97.2	0.591 (0.003)	0.10285 (0.00129)	1.975 (0.057)
CAP5_3	291 (16)	98.6	0.668 (0.010)	0.16443 (0.00054)	1.945 (0.006)
CAP5_4	239 (14)	98.1	0.500 (0.010)	0.09445 (0.00081)	1.449 (0.007)
CAP6_13	268 (15)	97.8	0.653 (0.012)	0.14264 (0.00099)	1.845 (0.009)
CAP6_20	265 (14)	97.2	0.622 (0.005)	0.13967 (0.00105)	1.836 (0.006)
CAP6_21	197 (11)	94.7	0.372 (0.003)	0.07624 (0.00069)	1.439 (0.006)
CAP7_26	299 (17)	95.4	0.545 (0.011)	0.13424 (0.00121)	1.605 (0.010)
AVC7_28	300 (16)	96.9	0.848 (0.009)	0.18595 (0.00134)	2.089 (0.016)
AVC7_29	244 (14)	97.1	0.721 (0.015)	0.20167 (0.00166)	2.729 (0.013)
AVC7_30	234 (13)	97.3	0.919 (0.013)	0.15818 (0.00166)	2.256 (0.014)

* The age of the Cima d'Asta Pluton (CAP) allanite and Atesina Volcanic Complex (AVC) allanite was calculated using La Posta Pluton (LPP) allanite as the standard with a defined 94 Ma age [$(^{208}Pb^*/Th)_s = 4.66 \times 10^{-3}$]. See Figure 12 for the 3-D calibration plot and Table 8 for a summary of this age data.
† The nomenclature indicates the grain and spot, respectively, of the analyzed allanite. See Figure 4 for some spot locations.

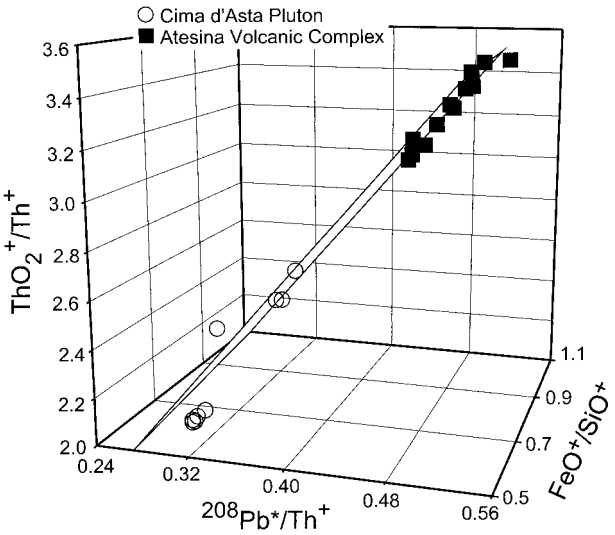

FIGURE 11. Calibration plane of $^{208}Pb^*/Th^+$ vs. ThO_2^+/Th^+ vs. FeO^+/SiO^+ for the Cima d'Asta Pluton and Atesina Volcanic Complex allanite grains. For numerical results, see Tables 6 and 8. These results represent two continuous days of analysis.

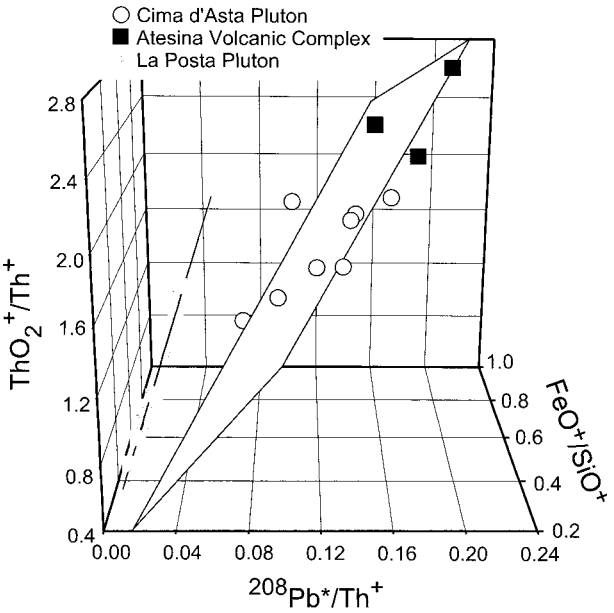

FIGURE 12. Calibration planes for the Cima d'Asta Pluton, Atesina Volcanic Complex, and La Posta Pluton allanite grains. For numerical results, see Tables 7 and 8. These results represent two continuous days of analysis.

TABLE 8. Summary table of the Th-Pb ion-microprobe age results for the Atesina Volcanic Complex (AVC), Cima d'Asta Pluton (CAP) allanite, and La Posta Pluton (LPP) allanite grains

Grain*	Average age (Ma)†	Accuracy (%)‡	MSWD§	All	B	C
			2-D calibration method#			
CAP (s)	273 (9)	±6	7.6			
AVC	137 (10)	±50	2.6			
			3-D calibration method**			
AVC (s)	276 (6)	±1	0.4	–0.043	0.172	–0.050
CAP	288 (6)	±6	6.4			
LPP (s)	94 (9)	±5	0.5	0.100	0.053	–0.026
AVC	259 (14)	±12	5.5			
CAP	250 (14)	±14	10.9			
CAP and AVC (s)	276 (8)	±2	0.8	–0.088	0.149	0.044

* A "(s)" following the grain name indicates this allanite was taken as the standard.
† Average age and 1σ errors listed in parentheses.
‡ The accuracy was calculated for each Th-Pb ion microprobe age {= [(age – known age)/known age] *100} and averaged.
§ MSWD = Mean Square Weighted Deviation calculated on the basis of 1σ error.
# The 2-D calibration method involves the ion-microprobe measurements of ThO_2^+/Th^+ and $^{208}Pb^*/Th^+$. The data for this block is listed in Table 5.
‖Coefficients A, B, C for the 3-D calibration plane calculated from a multivariate regression of several ion microprobe spots on the allanite standard grain.
** The 3-D calibration method involves ion-microprobe measurements of ThO_2^+/Th^+, $^{208}Pb^*/Th^+$, and FeO^+/SiO^+. The data for these blocks are listed in Tables 6, 7, and 9, respectively.

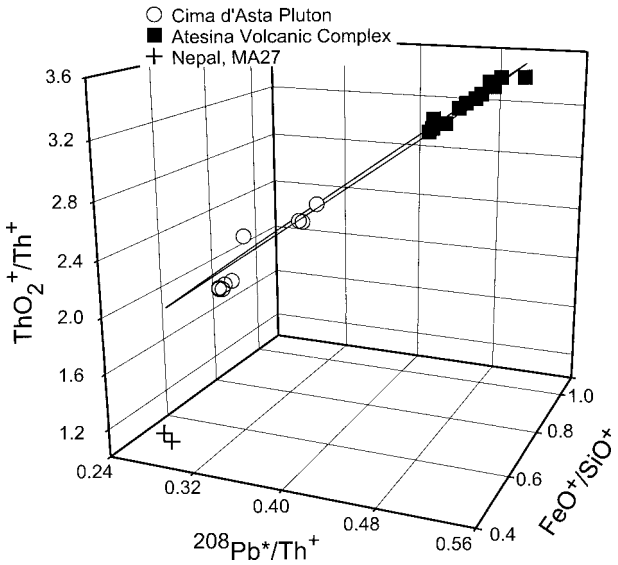

FIGURE 13. Calibration plane for the Cima d'Asta Pluton and Atesina Volcanic Complex. For numerical results, see Tables 8 and 9. These results represent one day of analysis.

probe measurements of coexisting monazite and allanite grains from the footwall of the Main Central Thrust.

Sample MA27 is structurally closer to the hanging wall (~0.2 km), whereas sample MA33 is ~8 km further south. The mineral assemblage for both samples is garnet + biotite + muscovite + chlorite + plagioclase + rutile + titanite. Sample MA27 contains matrix monazite and allanite inclusions in garnet grains, and sample MA33 contains monazite in both the matrix and garnet rims, but allanite only in garnet cores. Matrix monazite grains from sample MA27 yield a Th-Pb age of 17.7 ± 1.5 Ma (1σ; 4 spots on 1 grain), whereas MA33 matrix monazite and garnet-rim inclusions record Late Miocene crystallization at 6.8 ± 0.3 Ma (1σ; 3 spots on 3 grains).

Garnet-biotite thermometry (Ferry and Spear 1978; Berman 1990) and garnet-biotite-muscovite-plagioclase barometry (Powell and Holland 1988; Hodges and Spear 1982) yield temperatures and pressures for the garnet rim in MA27 of 640 ± 30 °C and 8.7 ± 0.8 kbar. The garnet rim of sample MA33 yielded lower pressures and temperatures of 565 ± 20 °C and 6.2 ± 0.4 kbar. We made compositional traverses for Mn, Mg, Ca, and Fe in garnets from these rocks to discern their zoning patterns. Sample MA27 garnets exhibit zoning in Mn, Mg, Ca, and Fe that are consistent with diffusion, whereas garnet zoning in sample MA33 is consistent with either a polymetamorphic history or a significant change of mineral assemblage. The garnet sharply decreases in Ca and Mn and increases in Mg and Fe within 0.2 mm of the rim. The ~7 Ma monazite inclusions in this sample are only found within these garnet rims.

TABLE 9. Th-Pb ion-microprobe age results for sample MA27 from Nepal using the 3-D calibration method and the Cima d'Asta Pluton (CAP) and Atesina Volcanic Complex (AVC) allanite as the standard*

grain_spot†	Age (Ma)	%^{208}Pb*	FeO^+/SiO^+	^{208}Pb*/Th$^+$	ThO_2^+/Th^+
AVC3_10	282 (8)	99.0	0.882 (0.008)	0.47203 (0.00253)	3.333 (0.022)
AVC3_11	274 (7)	99.1	0.930 (0.005)	0.42633 (0.00258)	3.144 (0.017)
AVC3_12	275 (11)	98.9	0.959 (0.029)	0.39619 (0.00245)	2.944 (0.012)
AVC3_13	275 (8)	99.4	0.932 (0.012)	0.47792 (0.00340)	3.476 (0.020)
AVC3_8	280 (8)	99.0	0.919 (0.006)	0.40471 (0.00306)	2.930 (0.023)
AVC3_9	270 (8)	98.0	0.813 (0.012)	0.41660 (0.00386)	3.041 (0.026)
CAP1_1	277 (8)	99.1	0.647 (0.006)	0.29641 (0.00247)	2.072 (0.009)
CAP1_2	272 (8)	99.1	0.580 (0.006)	0.29542 (0.00273)	2.059 (0.016)
CAP1_3	277 (8)	98.5	0.626 (0.005)	0.30437 (0.00326)	2.110 (0.019)
CAP1_4	272 (10)	99.2	0.504 (0.011)	0.32260 (0.00332)	2.198 (0.014)
CAP1_5	278 (9)	98.9	0.646 (0.005)	0.30659 (0.00379)	2.129 (0.024)
CAP1_6	265 (8)	98.6	0.530 (0.006)	0.30872 (0.00277)	2.178 (0.012)
CAP1_7	268 (8)	98.4	0.616 (0.007)	0.27995 (0.00197)	2.005 (0.020)
CAP2_17	300 (10)	98.3	0.547 (0.010)	0.33938 (0.00361)	2.126 (0.011)
MA27_1	458 (17)	77.0	0.404 (0.005)	0.02294 (0.00083)	1.146 (0.020)
MA27_2	432 (15)	76.3	0.409 (0.005)	0.02160 (0.00075)	1.190 (0.023)

* The age of the sample MA27 from Nepal was calculated using the Cima d'Asta Pluton (CAP) allanite and Atesina Volcanic Complex (AVC) allanite as the standard with a defined 276 Ma age [$(^{208}Pb^*/Th)_s = 1.37 \times 10^{-2}$]. See Figure 13 for the 3-D calibration plot and Table 8 for a summary of the standard allanite age data.

† The nomenclature indicates the grain and spot, respectively, of the analyzed allanite. See Figures 3 and 5 for some spot locations.

Allanite inclusions in MA27 garnet yielded ages that are significantly older than coexisting monazite, i.e., 445 ± 16 Ma (1σ; for 2 spots, see Table 9 and Fig. 13) vs. 252 ± 7 Ma (1σ; for 1 spot) for MA33. These results indicate that allanite formation in these rocks is not related to slip along the Main Central Thrust. Instead, allanite formation in these rocks may represent metamorphism associated with the older Pan-African orogeny (Le Fort et al. 1986) coupled with variable Pb loss. The result for MA33 is consistent with two-stage garnet growth and thus has implications for the timing and evolution of the inverted metamorphism that affected footwall rocks.

We also applied the 3-D calibration method to the analysis of an allanite grain from the Pacoima Canyon pegmatite, southern California, known informally as the "allanite pegmatite" (Silver et al. 1963) because of the high abundance of this mineral. This allanite is well known in mineralogical circles because it has been the subject of detailed structural studies (e.g., Dollase 1971). The Pacoima Canyon pegmatite contains large (several mm sized) euhedral allanite grains that appear to be unaffected by alteration. Our allanite sample was obtained from the Smithsonian Institution's National Museum of Natural History. Electron microprobe analyses indicate that the mineral contains ~1.1 wt% ThO_2. U-Pb isotope dilution analysis of zircon from the pegmatite yielded an age of 1191 ± 4 Ma (Silver et al. 1963; Barth et al. 1995). Using the LPP allanite as a standard, we obtained a Th-Pb age of 1006 ± 37 Ma (1σ; 2 spots on 1 grain). Although the age uncertainty is relatively large, our results suggest that cooling below the closure temperature for Pb diffusion in allanite occurred more than 100 million years following crystallization of the pegmatite.

Our data suggest that in situ Th-Pb ion-microprobe dating of allanite can be used to help solve problems that can be addressed with an age-dating accuracy of ±10%. This method permits in situ-dating of small (~15 μm) grains and grains included in phases such as garnet, with the spatial selectivity to analyze areas unaffected by alteration. Although the extreme compositional variability of allanite poses a challenge for ion-microprobe analysis because of matrix effects in sputtering yields, a 3-D calibration plot ($^{208}Pb^*/Th^+$ vs. ThO_2^+/Th^+ vs. FeO^+/SiO^+) can overcome this problem at a level of accuracy of about ±10%.

Acknowledgments

This project was supported by a Predoctoral Fellowship granted from the Smithsonian Institution's National Museum of Natural History and funding from the National Science Foundation. We acknowledge facility support from the Instrumentation and Facilities Program of the National Science Foundation. We thank Wayne Dollase, John Ferry, Trevor Ireland, Reto Gieré, and Stefan Claesson for reading and commenting on the manuscript, and David Virgo, Boz Wing, Marty Grove, and Jeremy Boyce for helpful discussions, Eugene Jarosewich for help obtaining the electron microprobe analyses, Chris Coath and John Ferry for help and insight into allanite ion-microprobe analysis and calibration development. We are particularly grateful to Felix Oberli for supplying the Northern Italian allanite samples.

References cited

Adams, J., Green, T.H., Sie, S.H., and Ryan, C.G. (1996) Trace element partitioning between aqueous fluids, silicate melts and minerals. European Journal of Mineralogy, 9, 569–584.

Affholter, K. (1987) Synthesis and crystal chemistry of lanthanide allanites. Virginia Polytechnic Institute and State University PhD Thesis.

Anders, E. and Grevesse, N. (1989) Abundances of the elements. Geochimica et Cosmochimica Acta, 53, 197–214.

Barth, A.P., Wooden, J.L., Tosda, R.M., Morrison, J., Dawson, D.L., and Hernly, B.M. (1995) Origin of gneisses in the aureole of the San Gabriel anorthosite complex and implications for the Proterozoic crustal evolution of southern California. Tectonics, 14, 736–752.

Barth S., Oberli F., and Meier, M. (1994a) Th-Pb versus U-Pb isotope systematics in allanite from co-genetic rhyolite and granodiorite: implications for geochronology. Earth and Planetary Science Letters, 124, 149–159.

———(1994b) Evidence for closed-system behavior of ^{232}Th-^{208}Pb in allanite under hydrothermal conditions: a study of altered rhyolite and granodiorite from the Atesina-Cima d'Asta volcano-plutonic complex (N. Italy). U.S. Geological Society Circular, 1107, 21.

Berman, R.G. (1990) Mixing properties of Ca-Mg-Fe-Mn garnets. American Mineralogist, 75, 328–344.

Bingen, B., Demaiffe, D., and Hertogen, J. (1996) Redistribution of rare earth elements, thorium, and uranium over accessory minerals in the course of amphibolite to granulite facies metamorphism: The role of apatite and monazite in orthogneisses from southwestern Norway. Geochimica et Cosmochimica Acta, 60, 1341–1354.

Broska, I. and Siman, P. (1998) The breakdown of monazite in the West-Carpathian Veporic orthogneiss and Tatric granites. Geologica Carpathica, 49, 161–167.

Buda, G. and Nagy, G. (1995) Some REE-bearing accessory minerals in two types of Variscan granitiods, Hungary. Geologica Carpathica, 46, 161–167.

Burt, D.M. (1989) Compositional and phase relations among rare earth element minerals. In Geochemistry and Mineralogy of Rare Earth Elements, Reviews in Mineralogy, 21, 259–30.

Campbell, F.A. and Ethier V.G. (1984) Composition of allanite in the footwall of the Sullivan Orebody, British Columbia. Canadian Mineralogist, 22, 507–511.

Chesner, C.A. and Ettlinger, A.D. (1989) Composition of volcanic allanite from the Toba Tuffs, Sumatra, Indonesia. American Mineralogist, 74, 750–758.

Clinkenbeard, J.P. and Walawender, M.J. (1989) Mineralogy of the La Posta Pluton: Implications for the origin of zoned plutons in the eastern Peninsular Ranges batholith, southern and Baja California. American Mineralogist, 74, 1258–1269.

Colchen, M., Le Fort, P., and Pecher, A. (1986) Annapurna-Manaslu-Ganesh Himal, 136 p. Centre National de la Recherches Scientifiques, Paris, France.

Compston, W. (1999) Geological age by instrumental analysis: the 29th Hallimond Lecture. Mineralogical Magazine, 63, 297–311.

Davis, D.W., Schandl, E.S., and Wasteneys, H.A. (1994) U-Pb dating of minerals in alteration halos of Superior Province massive sulfide deposits: syngenesis versus metamorphism. Contributions to Mineralogy and Petrology, 115, 427–437.

Dawes, R.L. and Evans, B.W. (1991) Mineralogy and geothermobarometry of magmatic epidote-bearing dikes, Front Range, Colorado. Geological Society of America Bulletin, 103, 1017–1031.

Deer, W.A., Howie, R.A., and Zussman, J. (1993) An Introduction to the Rock-Forming Minerals (2nd ed.). 696 p. Longman Scientific and Technical Press, Essex, England.

Dollase, W.A. (1971) Refinement of the crystal structure of epidote, allanite, and hancockite. American Mineralogist, 56, 447–464.

Dollase, W.A. and Newman, B. (1984) Statistically most probable stoichiometric formulae. American Mineralogist, 69, 553–556.

Drake, M.J. and Weill, D.F. (1972) New rare earth element standards for electron microprobe analysis. Chemical Geology, 10, 179–181.

Exley, R.A. (1980) Microprobe studies of REE-rich accessory minerals: implications for Skye granite petrogenesis and REE mobility in hydrothermal systems. Earth and Planetary Science Letters, 48, 97–110.

Ferry, J.M. and Spear, F.S. (1978) Experimental calibration of partitioning of Fe and Mg between biotite and garnet. Contributions to Mineralogy and Petrology, 66, 113–117.

Finger, F., Broska, I., Roberts, M.P., and Schermaier, A. (1998) Replacement of primary monazite by apatite-allanite-epidote coronas in an amphibolite facies granite gneiss from the eastern Alps. American Mineralogist, 83, 248–258.

Franz, G., Thomas, S., and Smith D.C. (1986) High-pressure phengite decomposition in the Weissenstein eclogite, Muenchberger Gneiss Massif, Germany. Contributions to Mineralogy and Petrology, 92, 71–85.

Gieré, R., Virgo, D., and Robert, K.P. (1999) Oxidation state of iron and incorporation of REE in igneous allanite. European Union of Geosciences 10, Journal of Conference Abstracts, 4, 721.

Green, T.H. and Pearson, N.J. (1983) Effect of pressure on rare earth element partition coefficients in common magmas. Nature, 305, 414–416.

Harrison, T.M., McKeegan, K.D., and Le Fort, P. (1995) Detection of inherited monazite in the Manaslu leucogranite by $^{208}Pb/^{232}Th$ ion microprobe dating: crystallization age and tectonic implications. Earth and Planetary Science Letters, 133, 271–282.

Harrison, T.M., Ryerson, F.J., Le Fort, P., Yin, A., Lovera, O.M., and Catlos, E.J. (1997) A late Miocene-Pliocene origin for Central Himalayan inverted metamorphism. Earth and Planetary Science Letters, 146, E1–E8.

Harrison, T.M., Grove, M., McKeegan, K.D., Coath, C.D., Lovera, O.M., and Le Fort, P. (1999) Origin and episodic emplacement of the Manaslu Intrusive Complex, Central Himalaya. Journal of Petrology, 40, 3–19.

Havette, A. (1985) Mineralogical application of the ion microscope elementary analy-

sis. Scanning Electron Microscopy, 2, 585–594.

Hodges, K.V. and Spear, F.S. (1982) Geothermometry, geobarometry and the Al_2SiO_5 triple point at Mt. Moosilauke, New Hampshire. American Mineralogist, 67, 1118–1134.

Hodges, K.V., Parrish, R.R., Housh, T.B., Lux, D.R., Burchfiel, L.H., Royden, L.H., and Chen, Z. (1992) Simultaneous Miocene extension and shortening in the Himalayan orogen. Science, 258, 1466–1470.

Hodges, K.V., Parrish, R.R., and Searle, M.P. (1996) Tectonic evolution of the central; Annapurna Range, Nepalese Himalayas. Tectonics, 15, 1264–1291.

Jarosewich, E. and Boatner, L.A. (1991) Rare earth element reference samples for electron microprobe analysis. Geostandards Newsletter, 15, 397–399.

Kingsbury, J.A., Miller, C.F., Wooden, J.L., and Harrison, T.M. (1993) Monazite paragenesis and U-Pb systematics in rocks of the eastern Mojave Desert, California, U.S.A.: implications for thermochronometry. Chemical Geology, 110, 147–167.

Lee, D.H. and Barston, H. (1967) Fractionation of rare-earth elements in allanite and monazite as related to geology of the Mt. Wheeler mine area, Nevada. Geochimica et Cosmochimica Acta, 31, 339–356.

Le Fort, P. (1996) Evolution of the Himalaya. In A. Yin and T.M. Harrison, Eds., The Tectonic Evolution of Asia, p. 95–109. Cambridge University Press, England.

Le Fort, P., Debon, F., Pêcher, A., Sonet, J., and Vidal, P. (1986) The 500 Ma magmatic event in Alpine southern Asia, a thermal episode at Gondwana scale. Sciences de la Terre, 47, 191–209.

Mezger, K., Hanson, G.N., and Bohlen, S.R. (1989) U-Pb Systematics of garnet: dating the growth of garnet in the Late Archean Pikwitonei granulite domain at Cauchon and Natawahunan Lakes, Maintoba, Canada. Contributions to Mineralogy and Petrology, 101, 136–148.

Oberli, F., Meier, M., Berger, A., Rosenburg, C., and Gieré, R. (1999) U-Th-Pb Isotope systematics in zoned allanite: a test for geochronological significance. European Union of Geosciences 10, Journal of Conference Abstracts, 4, 722.

Overstreet, W.C. (1967) The geologic occurrence of monazite. Geological Survey Professional Papers, 530, 1–327.

Peterson, R.C. and MacFarlane, D. (1993) The rare-earth-element chemistry of allanite from the Grenville Province. Canadian Mineralogist, 31, 159–166.

Petrík, I., Broska, I., Lipka, J., and Siman, P. (1995) Granitiod allanite-(Ce); substitution relations, redox conditions and REE distributions (on an example of I-type granitiods, Western Carpathians, Slovakia). Geologica Carpathica, 46, 79–94.

Powell, R. and Holland, T.J. (1988) An internally consistent thermodynamic dataset with uncertanties and correlations. 3. Applications to geobarometry, worked examples and a computer program. Journal of Metamorphic Geology, 6, 173–204.

Quidelleur, X., Grove, M., Lovera, O.M., Harrison, T.M., Yin, A., and Ryerson F.J. (1997) The thermal evolution and slip history of the Renbu Zedong Thrust, southeastern Tibet. Journal of Geophysical Research, 102, 2659–2679.

Ray, G. and Hart, S.R. (1982) Quantitative analysis of silicates by the ion microprobe. International Journal of Mass Spectrometry and Ion Physics, 44, 231–255.

Reed, S.J.B. (1985) Ion-probe determination of rare earths in allanite. Chemical Geology, 48, 137–43.

———(1986) Ion microprobe determination of rare earth elements in accessory minerals. Mineralogical Magazine, 50, 3–15.

Reed, S.J.B. and Buckley, A. (1998) Rare-earth element determination in minerals by electron-probe microanalysis: application of spectrum synthesis. Mineralogical Magazine, 62, 1–8.

Sawka, W.N., Chappell, B.W., and Norrish, K. (1984) Light-rare-earth-element zoning in sphene and allanite during granitiod fractionation. Geology, 12, 131–134.

Schmidt, M.W. and Thompson, A.B. (1996) Epidote in calc-alkaline magmas: An experimental study of stability, phase relationships, and the role of epidote in magmatic evolution. American Mineralogist, 81, 462–474.

Shimizu, N. and LeRoex, A.P. (1986) The chemical zoning of augite phenocrysts in alkaline basalts from Gough Island, South Atlantic. Journal of Volcanology and Geothermal Research, 29, 159–188.

Shimizu, N., Semet, M.P., and Allegre, C.J. (1978) Geochemical applications of quantitative ion-microprobe analysis. Geochimica et Cosmochimica Acta, 42, 1321–1334.

Silver, L.T., McKinney, C.R., Deutsch, S., and Bolinger, J. (1963) Precambrian age determinations in the western San Gabriel Mountains, California. Journal of Geology, 71, 196–214.

Smith, H.A. and Barreiro, B. (1990) Monazite U-Pb dating of staurolite grade metamorphism in pelitic schists. Contributions to Mineralogy and Petrology, 105, 602–615.

Sorensen, S. (1991) Petrogenetic significance of zoned allanite in garnet amphibolites from a paleo-subduction zone: Catalina Schist, southern California. American Mineralogist, 76, 589–601.

Srivastava, P. and Mitra, G. (1994) Thrust geometries and deep structure of the outer and lesser Himalaya Kumaon and Garhwal (India): Implications for evolution of the Himalayan fold-and-thrust belt. Tectonics, 13, 89–109.

von Blackenburg, F. (1992) Combined high-precision chronometry and geochemical tracing using accessory minerals: applied to the Central-Alpine Bergell intrusion (central Europe). Chemical Geology, 100, 19–40.

Walawender, M.J., Gastil, R.G., Clinkenbeard, J.P., McCormick, M.V., Eastman, B.G., Wernicke, R.S., Wardlaw, M.S., Gunn, S.H., and Smith, B.M. (1990) Origin and evolution of the zoned La Posta-type plutons, eastern Peninsular Ranges batholith, southern and Baja California. Geological Society of America Memoir, 174, 1–18.

Ward, C.D., McArthur, J.M., and Walsh, J.N. (1992) Rare earth element behavior during evolution and alteration of the Dartmoor Granite, SW England. Journal of Petrology, 33, 785–815.

Williams, C.T. (1996) Analysis of rare earth minerals. In A.P. Jones, F. Wall, and C.T. Williams, Eds., Rare Earth Minerals: Chemistry, Origin, and Ore Deposits, Mineralogical Society Series, 7, p. 327–346. Chapman and Hall, England.

Wing, B.A., Ferry, J.M., and Harrison, T.M. (1999) The age of andalusite and kyanite isograds in New England from Th-Pb ion microprobe dating of monazite. Geological Society of America, Abstracts with Programs, 27.

Zen, E. and Hammarstrom, J.M. (1984) Magmatic epidote and its petrologic significance. Geology, 12, 515–518.

MANUSCRIPT RECEIVED MARCH 9, 1999
MANUSCRIPT ACCEPTED DECEMBER 28, 1999
PAPER HANDLED BY BRAD L. JOLLIFF

View publication stats